VHMS mineralisation at Erayinia in the Eastern Goldfields Superterrane

VHMS mineralization at Erayinia in the Eastern Goldfields Superterrane: Geology and geochemistry of the metamorphosed King Zn deposit

Steven P. Hollis[1,2,3*], Darryl Podmore[4], Megan James[4], Julian F. Menuge[1], Aileen L. Doran[1], Christopher J. Yeats[2,5] & Stephen Wyche[3]

[1]iCRAG (Irish Centre for Research in Applied Geosciences) and School of Earth Sciences, University College Dublin, Belfield, Dublin 4, Ireland *E-mail: steve.hollis@icrag-centre.org
[2]CSIRO Earth Science and Resource Engineering, 26 Dick Perry Avenue, Kensington, Western Australia, 6151, Australia
[3]Geological Survey Division, Department of Mines and Petroleum, East Perth, Western Australia, 6004, Australia
[4]Black Raven Mining, PO Box 902, West Perth, Western Australia, 6872, Australia
[5]Geological Survey of New South Wales, NSW Department of Industry, 516 High St, Maitland, New South Wales, 2320, Australia

A manuscript for ***Australian Journal of Earth Sciences***
Keywords: volcanic-hosted massive sulfide; Archaean; Yilgarn Craton; lithogeochemistry; pXRF.

Abstract

Despite having been a target for volcanic-hosted massive sulfide (VHMS) deposits since the 1960s, few resources have been defined in the Archean Yilgarn Craton of Western Australia. Exploration challenges associated with regolith and deep cover exacerbate the already difficult task of exploring for small, deformed deposits in stratigraphically complex, metamorphosed volcanic terranes. We present results of drillcore logging, petrography, whole rock geochemistry and pXRF data from the King Zn deposit, to help refine mineralogical and geochemical halos associated with VHMS mineralization in amphibolite facies greenstone sequences of the Yilgarn Craton.

The King Zn deposit (2.15 Mt at 3.47% Zn) occurs as a 2-5m thick stratiform lens dominated by iron sulfides, in an overturned, metamorphosed volcanic rock-dominated sequence located ~140km east of Kalgoorlie. The local stratigraphy is characterized by garnet amphibolite and strongly banded intermediate to felsic schists, with rare horizons of graphitic schist. Massive sulfide mineralization is characterized by stratiform pyrite–pyrrhotite–sphalerite at the contact between quartz-muscovite schists ('the footwall dacite') and banded quartz-biotite/amphibole±garnet schists of the stratigraphic hanging-wall. A zone of pyrite-(sphalerite) and pyrrhotite–pyrite–(chalcopyrite) veining extends throughout the stratigraphic footwall. Footwall garnet-amphibolites are of sub-alkaline basaltic affinity, with a central zone dominated by chlorite±magnetite interpreted to represent the Cu-bearing feeder zone. SiO_2, CaO, Fe_2O_{3T}, MgO and Cu concentrations are highly variable, reflecting quartz–epidote±chlorite±magnetite±sulfide alteration. Hydrothermal alteration in stratigraphically overlying intermediate to felsic rocks is characterized by a mineral assemblage of quartz–

muscovite±chlorite±albite±carbonate. Cordierite and anthophyllite are locally significant and indicative of zones of Mg-metasomatism prior to metamorphism. Increases of SiO_2, Fe_2O_{3T}, pathfinder elements (e.g. As, Sb, Tl), and depletions of Na_2O, CaO, Sr, and MgO occur in footwall quartz-muscovite schists approaching massive sulfide mineralization.

Within all strata (including the immediate hanging-wall), the following pathfinder elements are strongly correlated with Zn: Ag, As, Au, Bi, Cd, Eu/Eu*, Hg, In, Ni, Pb, Sb, Se, Tl. These geochemical halos resemble less metamorphosed VHMS deposits across the Yilgarn Craton and suggest that although metamorphism leads to element mobility and mineral segregation at the thin section scale, assay samples of ~20cm length are sufficient to vector to mineralization in amphibolite facies greenstone belts. Recognition of minerals such as Mg-chlorite, muscovite, cordierite, anthophyllite, biotite/phlogopite, and abundant garnet are significant, in addition to Al-rich phases (i.e. kyanite, sillimanite, andalusite and/or staurolite) not identified at King. Chemographic diagrams may be used to identify and distinguish different alteration trends, along with several alteration indices (e.g. AI, CCPI, SI) and the abundance of normative corundum and quartz.

1. Introduction

For the last four decades, exploration for volcanic-hosted massive sulfide (VHMS) mineralization in the Archean Yilgarn Craton of Western Australia (**Fig. 1**) has been hampered by a perceived lack of prospectivity and difficult exploration conditions. The latter include deep and transported overburden, a paucity of outcrop, high strain, and saline groundwaters (McConachy et al. 2004; Yeats, 2007; Vearncombe, 2010; Hollis et al. 2015). In many greenstone belts, the proximity of supracrustal rocks to late stage granites, which comprise much of the craton, adds further complications. Metamorphic grade varies across the craton from greenschist to granulite facies, generally being higher closer to greenstone margins, and within narrower greenstone belts (e.g. Witt, 1991; Swager, 1997; Witt & Hagemann, 2012).

Few VHMS deposits have been identified in greenstone sequences metamorphosed to relatively high grade in the Yilgarn Craton (reviewed in Hollis et al. 2017a), as relatively simple primary alteration assemblages are often overprinted and obscured, with host rocks now comprising mineralogically complex banded schist or gneiss. For example, at Kingsley (the Wheatley prospect, South West Terrane: **Fig. 1**), massive sulfide mineralization is hosted at a transition between quartz-feldspar-biotite gneiss and hornblende-plagioclase-biotite-quartz±garnet amphibolite, marking a shift from felsic to mafic volcanism (Yeats, 2007; Hassan, 2017a). Sodium depletion in felsic gneisses underneath mineralization and the Al-rich minerals sillimanite, staurolite, kyanite and garnet provide evidence for a metamorphosed hydrothermal system (Yeats, 2007; Hassan, 2017a). In the eastern half of the Quinns district (Murchison Domain, Youanmi Terrane: **Fig. 1**), schistose rhyolite contains locally abundant and coarse-grained andalusite±kyanite±garnet where associated with VHMS mineralization (Duuring et al. 2016; Hassan, 2017b). The recognition of garnet and staurolite porphyroblasts for 30m above and below the Hollandaire deposit (Murchison Domain, Younami Terrane: **Fig. 1**) was also significant for VHMS exploration in the area (Hayman et al. 2015a).

Despite the increased difficulty of discovery, the metamorphism and deformation of VHMS deposits may bring economic benefits. These can include the significant upgrading and

redistribution of gold during metamorphism (e.g. Boliden deposit, Sweden; Wagner, et al. 2007), and the thickening of massive sulfide ores in hinge zones of folds (Dusel-Bacon, 2012). We present results of drillcore logging, petrography, whole rock geochemistry and pXRF data from the King Zn VHMS deposit in the Erayinia region of the southern Kurnalpi Terrane (Edjudina Domain, **Fig. 1**). We show that the mineralogical and geochemical signatures of the magmatic, hydrothermal and metamorphic events can be resolved. From these inferences we discuss features that may be used to identify VHMS deposits that have been metamorphosed at amphibolite facies in the Yilgarn Craton.

2. Geological setting

The Yilgarn Craton has historically been divided into a series of terranes based on distinct lithological associations, geochemistry and ages of volcanism (Gee et al. 1981; Myers, 1990; Cassidy et al. 2006). The western half of the Yilgarn Craton comprises the Narryer, South West and Youanmi terranes (**Fig. 1**). East of the Ida Fault, the Eastern Goldfields Superterrane (EGS) can be divided into the Kalgoorlie, Kurnalpi, Burtville and Yamarna terranes (Pawley et al. 2012; **Fig. 1**). The geology of the Yilgarn Craton with respect to VHMS mineralization has recently been discussed by Hollis et al. (2015; 2017a). Here we summarise the regional geology of the Kalgoorlie and Kurnalpi terranes (**Figs. 1 & 2**).

The geology of the Kalgoorlie Terrane is broadly divisible into the lower 2720-2690 Ma mafic-ultramafic Kambalda Sequence (Beresford et al. 2005) and the overlying 2690-2660 Ma Kalgoorlie Sequence (Krapež & Hand, 2008) (**Fig. 2**). At least two magmatic cycles, interpreted as plume related, are recognized in the lower sequence (Hayman et al. 2015b). The overlying 2690-2660 Ma Kalgoorlie Sequence comprises a >3km thick package of volcaniclastic rocks, felsic volcanic rocks, and mafic intrusive complexes with minor mafic volcanic rocks (Squire et al. 2010; **Fig. 2**). Late doming and extension associated with the emplacement of a widespread tonalite-trondjhemite-granodiorite (TTG) suite produced the late clastic basins of the Eastern Goldfields (Wyche et al. 2013; **Fig. 2**).

Broadly coeval with the Kambalda Sequence of the Kalgoorlie Terrane, the Kurnalpi and Minerie sequences of the Kurnalpi Terrane are represented by a more intermediate package of rocks (**Fig. 2**). Although some workers have attributed the Kurnalpi andesites to an Archaean arc (and thus the Kalgoorlie Terrane to a back-arc; e.g. Czarnota et al. 2010), they are also geochemically consistent with the fractionation of plume-related tholeiitic basalts, coupled with their contamination by contemporaneous partial melts of pre-existing continental crust (Barnes & Van Kranendonk, 2014). Between 2692 and 2680 Ma, volcanic centres in the Kurnalpi Terrane (Gindalbie Domain and further south; **Fig. 1**) are associated with largely bimodal (basalt-rhyolite) volcanic and associated sedimentary rocks, although some contain significant volumes of andesites (**Fig. 2**). These felsic rocks are significantly enriched in the high field strength elements (HFSE) and heavy rare earth elements (HREE) (Brown et al. 2002; Barley et al. 2008; Hollis et al. 2015), and are diagnostic of shallow crustal melting (Lesher et al. 1986; Piercey et al. 2001; Hart et al. 2004). This region of HFSE-enriched felsic volcanic rocks and broadly coeval HFSE-enriched granitic intrusions (Hollis et al. 2015) coincides with an area of juvenile crust revealed through regional Sm-Nd (granite; **Fig. 3**) and Pb isotope

(galena) variations (Huston et al. 2005, 2014). Interpreted as a paleo-rift zone, where juvenile material was added to the crust, similar isotopic features have also been recognized in the Youanmi Terrane (i.e. Cue Zone) and Abitibi-Wawa subprovince of Canada where they are associated with VHMS mineralization (Huston et al. 2014). To date only three VHMS deposits have been mined in the Eastern Goldfields Superterrane - all from the c. 2690 Ma Teutonic Bore volcanic complex (Hallberg & Thompson, 1985; Belford et al. 2015; **Fig. 3**). A significant resource of Ag-rich VHMS mineralization has also been recognized in the Kalgoorlie Terrane at Nimbus (**Fig. 3**), interpreted to represent a shallow water and low temperature deposit formed on the margin of the Kurnalpi rift zone at c. 2705 Ma (Hollis et al. 2017b).

3. Regional Geology of Erayinia

The regional geology of the Erayinia area in the southern Kurnalpi Terrane is detailed in the 1:100,000 GSWA explanatory notes (Jones, 2007). Two major faults (Claypan and Roe Hills) divide the area into three domains - Edjudina, Murrin and Menangina (**Fig. 4**). As the Edjudina Domain at King is the focus of this paper, the other two domains will not be discussed. An account of VHMS mineralization in the Murrin Domain ~4km NW of King will be presented elsewhere (Hollis et al. in prep).

The Edjudina Domain across its ~300km length (**Fig. 1**) is dominated by several basaltic to rhyolitic volcanic complexes, and laterally extensive belts of intermediate schist predominantly derived from andesitic precursors (Swager, 1995, 1997). Prominent, though volumetrically minor, marker beds of banded iron formations (BIF), chert and fine grained metasedimentary rocks cap the aforementioned sequence, which are intruded by extensive dolerite sills (Swager, 1995, 1997). A narrow eastern belt of thin basalt which contains komatiite layers was also recognized. Existing U-Pb zircon ages from the southern half of the Edjudina Domain are limited to: i) 2708 ± 6 Ma from a fragmental metadacite porphyry in a felsic sequence associated with calc-alkaline rocks ~100km N of King (Nelson, 1995); ii) 2698 ± 10 Ma from a metatonalite intrusion also ~100km N of King (Nelson, 1996); and iii) 2680 ± 4 Ma from a granite gneiss at Coonana Hill ~30km NE of King (Wingate et al. 2016). The distribution of komatiite and BIF with in the southern Eastern Goldfields, along with all current U-Pb zircon ages from the region, is shown in **Figure 5**.

Jones (2007) provides a more local summary of the geology at Erayinia east of the Claypan Fault (**Fig. 4**). According to Jones (2007), greenstone sequences contain interlayered mafic and felsic schists, ferruginous chert bands and silicified black shales that define tight folds on aeromagnetic images. Further east, along the eastern margin of Erayinia, thin units of meta-ultramafic rocks (komatiite?) and metabasalt are interlayered with metasedimentary rocks (**Fig. 4**). The mapped meta-ultramafic rocks are preserved as deeply weathered talc-chlorite-(carbonate) schists ~17 SE of King (**Fig. 4**) (Jones, 2007). Together with the presence of a large rubbly outcrop of Fe-rich chert ~10km N of King, that is similar in appearance to BIF (Jones, 2007), this may suggest the local stratigraphy is >2.7 Ga in age and belongs to the Minerie or Kurnalpi sequence (**Fig. 2**). The Gindalbie age (2680 ± 4 Ma) from a 'granite gneiss' at Coonana Hill ~30km NE of King (Wingate et al. 2006; **Fig. 5**) may belong to a similar sequence to the 'schist derived from granite rock' mapped by Jones (2007) in **Figure 4**.

Unfortunately, our attempted U-Pb dating of the King stratigraphy was unsuccessful due to a paucity of zircons recovered from footwall quartz-muscovite schists.

Regional deformation of the Erayinia region is complex and typically involved an early extensional event (D_E), followed by: D_1 compression involving thrusting and recumbent folding (F_1); D_2 ENE-WSW crustal shortening, producing major upright folding (F_2: 2675-2657 Ma); D_3 sinistral movement and associated folding on NNW-trending regional strike slip faults; and D_4 overprinting with oblique reverse movements on the same structures (Jones, 2007).

Peak metamorphism across the Eastern Goldfields is most intense (upper amphibolite facies) surrounding large granitoid bodies that were emplaced at 2660-2640 Ma, broadly contemporaneous with D_2 deformation (Witt, 1991; Nelson, 1997; Swager et al. 1997). Away from these granitoids, porphyroblasts of biotite and andalusite grew over and across the vertical regional foliation indicating the relatively late timing of peak regional metamorphic conditions (Swager, 1997). Lower grade zones of greenschist facies metamorphism are found in the central parts of greenstone belts (Jones, 2007). A marked increase in metamorphic grade was noted by Jones (2007) across the Claypan Fault (**Fig. 4**), from relatively undeformed greenschist facies felsic volcaniclastic rocks and basalt in the west, to muscovite schist, chlorite-muscovite schist, and biotite-garnet schist east of the fault.

4. King deposit stratigraphy

The King Zn deposit (~2.146 Mt at 3.47% Zn, non-compliant at 1% cut off) occurs in an overturned and east-dipping volcanic-dominated sequence (**Fig. 6**) located approximately 140km east of Kalgoorlie (**Fig. 1**) and 36km south of the Trans Australian Railway. Although the area had previously been explored for uranium and gold, base-metal mineralization was first targeted during the 1990s by Sons of Gwalia. Following geological mapping, ground magnetometry and surface TEM geophysics, a conductor was recognized as coincident with a magnetic anomaly. Further soil sampling and Reverse Circulation (RC) drilling led to the interception of narrow massive sulfide layers at King (formerly called Calliope). The most extensive exploration activity was undertaken by ABM Resources from 2005 to 2012 as the manager of a joint venture with Hawthorn Resources Ltd (detailed in Podmore & James, 2016). Subsequent diamond, RC and Rotary Air Blast (RAB) drilling by ABM defined the current size of the King deposit (**Figs. 6a, b**). More recently, a soil and rock chip sampling programme, and VTEM (Versatile Time Domain EM) geophysical survey, was undertaken by Black Raven Mining (2012-2017) over the extended licence areas.

Our current interpretation is that the volcanic stratigraphy at King is overturned and dipping to the east (**Fig. 6c**). This is based on metal zonation in the deposit, and the distribution and intensity of logged hydrothermal alteration assemblages (see Discussion). An intensely chloritized zone of discordant alteration with abundant chalcopyrite and Fe-sulfides lies above a sheet-like body of massive Fe-Zn sulfide (**Fig. 6d**), the opposite to most VHMS systems (Hannington et al. 2005; Galley et al. 2007). Graded were beds also noted by ABM geologists from drilholes EC120D and EC116D (ABM Resources NL, 2008) consistent with our

interpretation, although these have not been verified since. Possible graded bedding from hole EC056D is shown in **Figure 7l**. An overturned stratigraphy is also consistent with Swager's (1995, 1997) description of rocks from the Edjudina domain - namely basaltic to felsic volcanic complexes, overlain by fine grained sedimentary rocks, chert and BIF intruded by mafic sills – and also a recent study from King North (Kelly, 2018, unpublished thesis; **Fig. 4**).

Photographs of the main lithologies and styles of mineralization present in diamond drillcore are shown in **Figures 7 and 8**. The stratigraphy at the King deposit from interpreted stratigraphic footwall to hanging-wall, assuming an overturned stratigraphy (**Fig. 6c**), is characterised by:

***Footwall garnet-amphibolite*:** A thick (>300m) sequence of foliated garnet-amphibolite or hornblende-garnet-quartz schist (**Figs. 7ab, 9a**) occurs in the deep stratigraphic footwall of the King deposit, with the top contact now ~100-150m above mineralization (**Fig. 6c**). The groundmass is dominated by fine granulose green hornblende with interstitial fine anhedral quartz, minor epidote, and carbonate (**Fig. 9a**). Garnet porphyroblasts contain quartz and hornblende inclusions. A general anastomosing schistosity (**Fig. 7b**) is paralleled by the granulose hornblende texture. Local zones with abundant ragged and acicular actinolite (to ~3mm in drillcore) also occur. Towards the centre of the King deposit a zone characterized by abundant chlorite is present (**Figs. 6d, 9d**). This is best observed in drillhole EC116D where fine magnetite crystals are disseminated throughout the core in close association with chalcopyrite±pyrite blebs and stringers (**Figs. 8a-b, 9b-c**). Contacts are gradational with surrounding garnet-amphibolites, with the change in rock type reflecting an increased abundance of chlorite±magnetite to hornblende-garnet-quartz.

The thick sequence garnet-amphibolite is interpreted to represent a sheared and metamorphosed sequence of mafic rocks. It is unclear due to the strong banding and recrystallization whether these represent metamorphosed coherent mafic flows, volcaniclastic rocks or thick basaltic sills. Primary volcanic textures such as pillows, varioles, chilled margins and peperite are not preserved. Similar mafic lithologies have been mapped by Jones (2007) along strike to the north of the King deposit (weakly foliated amphibolite; **Fig. 4**). Quartz and epidote altered mafic volcanic rocks (greenschist facies) have also been recently drilled at King North along strike (**Fig. 4**), which are geochemically similar to those described here (Kelly, 2018, unpublished thesis). The zone of intense chlorite with Cu-Fe sulfides is interpreted to represent the feeder zone to massive sulfide mineralization that was enriched in Mg prior to metamorphism (see Discussion).

Mixed footwall sequence: Stratigraphically overlying the garnet amphibolite is a ~30 to 130m thick mixed sequence of intensely altered, intermediate to felsic schist. Rare units (<15m thick) resembling the aforementioned footwall garnet-amphibolite also occur. Rocks of the mixed footwall sequence are highly variable in their mineralogy and are strongly banded and folded (**Figs. 7d-g**). More leucocratic (intermediate to felsic) lithologies are dominated by a combination of quartz, chlorite and carbonate with lesser hornblende, biotite and epidote (**Figs. 9e-h**). Where present, biotite parallels the schistosity and is often retrogressed to chlorite. Leucoxene, zircon and titanite are present as accessory phases. Zones rich in albite and/or

muscovite also occur. In the rare mafic lithologies, the metamorphic matrix is dominated by hornblende with minor epidote in darker bands, and quartz-epidote-chlorite in paler bands.

Throughout each of the drillholes logged at the King deposit (**Fig. 6a**) a distinct zone of intense brown and green banding is common (**Fig. 7d**). This occurs at depths anywhere from ~50 to 150m in the footwall to massive sulfide mineralization and varies in thickness from a few metres to tens of metres. This lithology is characterized by quartz, anthophyllite, clinozoisite and biotite (intergrown with anthophyllite and replaced by chlorite) (**Fig. 9f-h**).

The mixed footwall sequence is interpreted to represent a package of metamorphosed intermediate to felsic volcaniclastic rocks, with rare mafic sills/lava flows (now garnet-amphibolite) and thin beds of deep marine argillaceous sediments (typically <2m thick; preserved as graphitic schist; see section below). Rare examples of lapilli tuff have been described from this sequence, with relict quartz clasts apparent in thin section. The zone rich in anthophyllite is interpreted to reflect Mg-metasomatism prior to metamorphism in the intermediate to felsic lithologies.

Quartz-muscovite schist (footwall dacite): A ~50 to 90m thick sequence of leucocratic and variably banded quartz-muscovite schist of dacitic composition comprises the immediate stratigraphic footwall to massive sulfide mineralization at King (**Figs. 6c, 7h**). In some instances, coherent and weakly altered units occur in close proximity to mineralization, surrounded by intensely altered and sheared lithologies. Quartz-muscovite schists are dominated by fine granoblastic quartz with interstitial platy muscovite defining the schistosity (**Figs. 9i-j**), and minor epidote. Locally, Mg-rich cordierite can be significant (≦5%) as aggregates and crystals throughout the matrix. This is often replaced by sericite and associated Mg-chlorite. Bands of sericitised plagioclase occur in the matrix of some samples. Sulfides, tourmaline, hornblende, leucoxene and zircon are present as accessory phases (**Fig. 9k**). Garnets are rare, but small (<2mm) pink to red porphyroblasts are disseminated throughout most units logged. Directly under massive sulfides (**Fig. 9l**, described in **Section 5**), the quartz-muscovite schists are intensely silicified in hand specimen. With depth, an increase in muscovite, chlorite and albite is clear in drillcore (**Fig. 6c**). Contacts between different styles of alteration are gradational. Where present, pyrite and sphalerite occur as stringers and disseminated throughout the host stratigraphy (**Figs. 8c, 9k;** see **Section 5**).

The thick sequence of quartz-muscovite schist is interpreted to represent a mixed, hydrothermally altered and metamorphosed sequence of dacitic volcaniclastic rocks and more coherent volcanic lithologies (either representing flows or high-level intrusions). No quartz or feldspar phenocrysts were observed; all rocks examined in thin section are strongly recrystallized and show evidence of shearing.

***Mixed hanging-wall sequence*:** The immediate hanging-wall of the King deposit is dominated by finely banded (mm to cm scale) schists of mafic to felsic composition (**Fig. 7i**), grouped together here as quartz-biotite/amphibole±garnet schists. Banding reflects the varying

abundance of fine to medium granoblastic quartz (with lesser biotite) to tremolite/actinolite±garnet (**Figs. 9o-p**). Garnet can be retrogressed to fibrous chlorite aggregates with quartz. Calcite is present throughout the matrix, as well as in veinlets and vugs (**Figs. 9q-r**). Magnetite is disseminated (3-5%) throughout the matrix of the banded schists directly overlying massive sulfides (**Fig. 6**). In the deeper sections of the deposit where magnetite has not been replaced by secondary Fe-oxides, a very strong magnetic signature persists for ~1 to 4m into the stratigraphic hanging-wall. This zone is typically more magnetic than the pyrrhotite-magnetite-bearing chloritic feeder zone, but the intensity of both varies significantly from hole to hole. Pyrite stringers are abundant close to massive sulfides and are strongly recrystallized. These pyrite parallel and cut metamorphic banding at high angles (**Fig. 8f**). The most convincing example of grading, shown in **Fig. 7l**, is consistent with an overturned stratigraphy.

Thin horizons of graphitic schist (described below), pyrite-bearing polymict volcanic breccias (**Fig. 7k**), and rare, coherent carbonate-altered rocks of mafic composition (herein termed the hanging-wall amphibolites) are also present in the stratigraphic hanging-wall to mineralization. The hanging-wall amphibolites (~3m thick) are dominated by amphibole and quartz, with carbonate alteration and relict clinopyroxene. Garnets can be present, but not in every drillhole. Finely banded chert-like rocks were noted at ~385m depth in drillhole EC056D (**Fig. 7j**). The polymict volcanic breccias (~382m in EC056D) are intensely brecciated, quartz veined, contain clasts up to 4cm of surrounding lithologies (e.g. layered chert, banded schist, amphibolite), and thin stringers of magnetite.

The mixed hanging-wall sequence is interpreted to represent a sequence of metamorphosed interbedded volcanic/volcaniclastic rocks of varying composition, with interbedded fine grained, deep marine sedimentary rocks. The hanging-wall amphibolites may represent very thin lava flows or coeval basaltic sills (e.g. Swager, 1997).

Horizons of graphitic schist: Thin (0.4-2m) horizons of graphitic schist have been identified throughout the King stratigraphy in both the interpreted footwall (ED086 303m) and hanging-wall (ED143 ~505m) to massive sulfide mineralization. Similar lithologies were also noted as deformed fragments within the massive sulfide zone of drillhole EC116D, where they are intensely chloritized and in some sections appear to have been replaced by sulfides. The horizons of graphitic schist are always intensely fractured, strongly sheared, and can be intermittently banded with surrounding lithologies (e.g. garnet amphibolite, quartz-muscovite schists). In most instances fault gouges are closely associated with the graphitic schists, indicative of thrusting in the stratigraphy. The graphitic schists most likely represent metamorphosed deep marine argillaceous sediments precipitated under anoxic conditions.

***Quartz-feldspar phyric intrusive rocks*:** The King stratigraphy has been intruded by at least two generations of quartz-feldspar porphyry sills that broadly parallel bedding (**Fig. 6**). The earlier set appears to be broadly coeval with the volcanic stratigraphy and are ~0.7 to 1.5m thick with sharp margins (e.g. at 309m EC056D; 387m EC116D). They exhibit a similar mineralogy (quartz-muscovite) to the footwall felsic rocks they intrude, contain disseminated

sulfides, and have a strong foliation which parallels surrounding strata (**Fig. 6c**, labelled 1; **Fig. 7m**).

A presumably younger set of thinner (5-30cm) quartz-feldspar phyric sills intrude the hanging-wall to massive sulfide mineralization in hole EC056D (~363m; **Fig. 6c**, labelled 2). This suite is less foliated (**Fig. 7n**) and resemble those of the Erayinia NW area closely associated with late high-Ca granitoid intrusions of the eastern Murrin Domain (Hollis et al. in prep). Sharp unchilled margins are orientated parallel to banding in surrounding schists.

Late basaltic dykes: Late basaltic dykes crosscut the stratigraphy and are undeformed. These rocks are typically ~0.5 to 2.5m thick, coarsen to doleritic centres, and display chilled margins and varioles (**Fig. 7o**). They most likely belong to the Palaeoproterozoic Widgiemooltha Dyke Suite (**Fig. 6**). The suite is clearly visible in regional magnetics and intrudes the area in predominantly E-W and NNE-SSW orientations (**Fig. 4**).

5. Sulfide mineralization at King

Sulfide mineralization at King occurs predominantly as a stratiform, ~1 to 7m thick, sheet-like body of massive pyrite-pyrrhotite with subordinate sphalerite, at the contact between intensely silicified dacite (footwall quartz-muscovite schist) and banded quartz-biotite/amphibole±garnet schist (**Fig. 6c**). This zone of stratiform massive sulfide mineralization dips at 45-70° eastwards, has a confirmed depth of at least 400m, and has been drilled across a strike length of ~600m (**Fig. 6a**). Diamond drilling is restricted to the central 450m (**Fig. 6a**). Two small, high-grade lenses of Zn mineralization have been recognised separated by a central zone (150-200m long) with lower Zn grades (**Fig. 6b**). The best intercept is 5m at 10.6% Zn in drillhole EC116D. There has been sporadic analysis for gold in both massive sulfides and the feeder zone. Significant intercepts include 5m at 0.6 g/t Au (hole EC046D) and 5.9m at 0.3g/t Au (EC031D) (**Fig. 6b**). Stratigraphically underlying the stratiform massive sulfides a zone of discordant vein and disseminated sulfides (from pyrite-sphalerite to pyrrhotite-chalcopyrite-pyrite; **Fig. 8a-b**) extends throughout the underlying strata (**Fig. 6d**). It is important to note that all sulfide assemblages show evidence for recrystallization.

Within the massive sulfides two broad styles of mineralization can be defined: a lower zone characterized by fine to coarse grained subhedral pyrite with replacive interstitial red/brown sphalerite (**Fig. 8d**), and a stratigraphically overlying zone dominated by iron sulfides (pyrite and/or pyrrhotite) with large milled clasts of surrounding lithologies (**Figs. 8e**, **9l-n**). In the stratigraphically lower Zn-rich zone, abundant fine to coarse grained subhedral pyrite is replaced by sphalerite (**Figs. 8d, 9l**). Anhedral quartz and Fe-chlorite are interstitial to sulfide phases. Pyrrhotite is concentrated locally in the matrix. Galena is rare, and is present both as rims to, and inclusions in, pyrite. Tetrahedrite locally replaces galena and exhibits simple intergrowths with sphalerite.

In the overlying Fe-rich zone, pyrite and/or pyrrhotite are typically the dominant sulfide phase with subordinate sphalerite and rare galena. Chalcopyrite inclusions occur in pyrrhotite. Siliceous clasts of varying size are present in the sulfide matrix. These are well rounded and

represented by quartz-muscovite schist derived from the underlying footwall, or schist from the stratigraphic hanging-wall (**Figs. 9m-n**). Garnet in the hanging-wall schist fragments is retrogressed to chlorite (**Fig. 9n**). In drillhole EC116D, abundant fragments of chloritized and deformed graphitic schist are within the massive sulfides.

Silicified felsic footwall rocks immediately underlying massive sulfides contain veinlets of pyrite-sphalerite, which become more sphalerite poor with depth. These are often strongly sheared, with trails of coarse euhedral pyrite orientated parallel to metamorphic banding (**Fig. 8c**), and the contact with overlying massive sulfides (**Fig. 8d**). When present, sphalerite occurs interstitially to euhedral pyrite (**Fig. 9k**), with both phases cut by veinlets of galena.

In the chlorite-rich zone of garnet-amphibolite (**Fig. 6d**) chalcopyrite is most common as blebs and stringers, along with veinlets and individual crystals of pyrrhotite and pyrite (e.g. EC116D; **Figs. 8a-b**). Sphalerite crystals are often strongly deformed and may be intergrown with both chalcopyrite and pyrrhotite. Ilmenite ($FeTiO_3$) occurs as exsolution lamellae in the coarse magnetite grains, and as individual crystals in pyrrhotite (**Fig. 9b-c**). Pentlandite ($[Fe,Ni]_9S_8$) is rare and is intergrown with pyrrhotite. Chalcopyrite is also intergrown with pyrrhotite and fills fractures in magnetite grains (**Fig. 9c**). Drillcore logging also revealed that secondary Cu minerals (predominantly malachite) are present in the uppermost sections of the King deposit, most likely remobilised from the underlying Cu-bearing chloritic stockwork.

The immediate hanging-wall above massive sulfides can contain abundant stringers of coarse euhedral pyrite (**Fig. 8g**) orientated both along the main foliation and crosscutting brecciated hanging-wall lithologies.

6. Geochemistry

6.1. Methods

Whole rock lithogeochemistry

A total of twenty-three samples of diamond drillcore from the King stratigraphy (holes EC116D, EC031D, EC056D; **Fig. 6c**) were analysed for whole rock geochemistry at ALS Laboratories, Perth, Australia. Major element concentrations were determined by four acid digestion and ICP-OES finish on fused glass beads. Trace element, HFSE and REE concentrations were determined by lithium borate fusion and ICP-MS finish. Base metals (e.g. Cu, Pb, Zn, Ni) and trace metals (e.g. As, Sb, Tl, Bi) were analysed by multi-acid digestion, followed by ICP-OES and ICP-AES, respectively. Carbon and S concentrations were determined by total combustion using a Carbon-Sulfur Analyser, and LOI using a robotic thermo-gravimetric system. Gold, Pt and Pd concentrations were analysed by fire assay and ICP-OES.

Accuracy (%RD) was monitored using laboratory blind, mineralized and unmineralized international standards (e.g. OREAS-24b – granodiorite, OREAS-620 – Golden Grove ore). Precision (%RSD) was monitored by repeat analysis of submitted standard OREAS-24b

(granodiorite). Both precision and accuracy are considered excellent to good after Jenner (1996; i.e. within ±10% RSD and <10% RD) for the majority of elements from both datasets. W, Li, Sn and Mo data was discarded due to poorer accuracy and/or precision than the other elements (consistently >10% RD to international standards). Thallium data was retained due to excellent precision (<1% RSD), but absolute values here should be treated with caution as accuracy was poor (>30% RD). Whole rock geochemistry results are presented in **Supplementary Table 1** and plotted in **Figures 10 to 13**.

Portable X-ray Fluorescence geochemistry

The above whole rock geochemical data from the King deposit is complemented by ~620 portable X-ray Fluorescence (pXRF) measurements on diamond drillcore (5 holes). Portable XRF measurements were made every 0.5 to 2m of core (dependent on hole length) using an Olympus InnoveX Systems Delta 2012 series model between March and May 2015. The counting time was 60 seconds per analysis in soil mode. Several studies using international reference materials have shown pXRF data to be precise for a number of major and trace elements (e.g. Piercey & Devine, 2014). Although the accuracy of pXRF data ranges widely from excellent (<7% RD) to poor (±20% RD), and often needs correcting (e.g. Fisher et al. 2014; Le Valliant et al. 2014), downhole profiles replicate the geometry of those obtained from conventional analyses (Piercey & Devine, 2014). Such data is fit-for-purpose and useful for enhancing downhole geochemical trends obtained by conventional methods but should not be used as a substitute for high-quality lithogeochemistry (Piercey & Devine, 2014).

pXRF data was corrected using eleven standards from OREAS (OREAS-22d, 24b, 24c, 36, 38, 70b, 76b, 291, 931, 935, 991) for the following elements: As, Cr, Cu, Fe, Mn, Ni, Pb, Rb, Sr, Ti, V, Y, Zn, Zr. These standards cover a wide range of concentrations for each element (e.g. 38 ppm to 12.4% Cu, 4.45-23.6 wt% Fe). Calibration equations were obtained by plotting certified concentrations against obtained pXRF values for each element. Only standards that returned pXRF values above the limit of determination (LOD: 3x detection) were used in each equation. This process was done separately for each drillhole. As an increase in pXRF machine internal temperature (and consequently air pressure) is known to cause instrument drift over time (due to peak positions migrating; Fisher & Gazley, 2014), standard OREAS-24b was analysed every 15-20 spot analyses (total n=71 for 5 holes). Apart from single point anomalies, instrument drift was found to be negligible and non-systematic.

Calibration equations used to correct pXRF data are provided in **Supplementary Table 2** along with R^2 values, which were generally excellent (most >0.98) apart from for Cr and V (which were rarely above LOD). Slight offsets between corrected pXRF and lithogeochemical datasets are to be expected due to the effect of spot analysis (~10mm diameter) on heterogeneous drillcore (Fisher & Gazley, 2014), and attenuations of elements by the plastic bags in which standards were analysed (see Fisher et al. 2014). That said, these combined effects appear to be minimal here for the elements of interest. Our corrected pXRF data closely follow data obtained by conventional lithogeochemical methods. Calculated precision and accuracy data for standard OREAS-24b is presented in **Supplementary Table 3** following the correction of each element. Note the excellent data quality for Sr and Rb regardless of date,

poorer data quality for As regardless of date, and reduced precision for all elements on the 14th of May, 2015 (drillhole EC056D; most likely due to the pXRF overheating). The following elements reported by the pXRF were discarded: Ag, Au, Bi, Hf, Sb, Sn, Mo, Th, U, W. These were rarely above LOD and were associated with large errors (e.g. Ag ± 9 ppm, Sb ± 20 ppm). Corrected pXRF data is presented in **Supplementary Table 4**.

Magnetic susceptibility

Magnetic susceptibility measurements were taken systematically every 1m of diamond drillcore logged on metre marks using a Fugro RT-1 Magnetic Susceptibility Meter (~2000 measurements from 10 holes).

6.2. Immobile element geochemistry

The mobility of most of the major and trace elements during hydrothermal alteration is well established in the literature (e.g. MacLean, 1990; Jenner, 1996). Only the following elements, that are demonstrably immobile during both hydrothermal alteration and amphibolite-facies metamorphism, are used here to elucidate petrogenesis: Al_2O_3, TiO_2, Th, Co, V, the HFSE (e.g. Nb, Y, Sc) and REE (minus Eu) (Pearce & Cann, 1973; MacLean, 1990; Jenner, 1996). While these elements may move on the millimetre scale during hydrothermal alteration and subsequent metamorphism (as they are transferred into new minerals), they can be considered immobile at the hand-specimen scale and particularly in sections of drillcore analysed here (~20cm length).

The immobile element geochemistry of samples analysed from the King deposit is illustrated in **Figures 10 and 11**. All samples of garnet-amphibolite from the footwall of the deposit (and thin amphibolite units from the hanging-wall) are of calc-alkaline basaltic affinity according to both the Zr/TiO_2 vs Nb/Y classification diagram of Pearce (1996; **Fig. 10a**), and the Co vs Th diagram of Hastie et al. (2007; **Fig. 10d**). One exception is sample GK021, which displays more intermediate geochemical characteristics (**Fig. 10a**). This is consistent with its position near the overlying mixed footwall sequence (**Fig. 6c**) that is dominated by more siliceous rocks. Footwall garnet-amphibolites are generally characterised by consistently high Sc (17-46 ppm) and Co (84-119 ppm) concentrations, and variable Cr (<10-150 ppm) and immobile element ratios (e.g. Zr/Y 2.2-12.8). Chondrite normalized REE profiles show little variation between units in terms of the HREE (Dy/Yb 1.4-1.9), but there is significant LREE variation in the samples analysed (La/Yb 1.7-16.5; **Fig. 11d**). This may be a consequence of LREE mobility in the intensely chloritized feeder zone underlying massive sulfides (e.g. Barrett & MacLean, 1994). Two samples of amphibolite analysed from the hanging-wall of the King deposit (**Fig. 6c**) contain lower Co concentrations (**Fig. 10d**), higher Zr/TiO_2 ratios (**Fig. 10a**) and similar chondrite normalized HREE profiles to those from the footwall (**Fig. 11d**).

Rocks of intermediate composition from the mixed footwall sequence display gently dipping REE profiles (La/Yb 5.8-9.1; **Fig. 11e**). Zr/TiO_2 ratios, and concentrations of Th, Sc and Co are similar to overlying quartz-muscovite schists at King (**Fig. 10b**). Niobium, Y, Hf and Zr concentrations are generally higher in the intermediate volcaniclastic rocks than

493 overlying felsic rocks; however, this may be a function of higher mass gain in the quartz-
494 muscovite schists, as ratio combinations of these elements yield similar values.

495 Quartz-muscovite schists from the immediate footwall of the King deposit are
496 characterised by andesitic to dacitic Zr/TiO_2 ratios (223-284; **Fig. 10b**), and calc-alkaline Zr/Y
497 (4.6-15.0) and La/Yb ratios (>9.0). Cr concentrations are below detection (<10 ppm), and Co
498 concentrations are generally low (**Fig. 10d**), both of which are consistent with a dacitic
499 protolith. Low HFSE concentrations (<5.7 ppm Hf, 5.3-15.7 ppm Y, <0.4 ppm Ta) indicate
500 these rocks are of FI (to FII) affinity (**Fig. 10e-f**). Chondrite normalized REE profiles have
501 intermediate characteristics between felsic rocks from Nimbus and Teutonic Bore (**Fig. 11f**).

502 Hanging-wall banded schists range in composition from mafic to felsic according to
503 their Zr/TiO_2 ratios and Co concentrations (**Fig. 10c, d**), consistent with their variations in
504 mineralogy (quartz-biotite dominated to amphibole±garnet) (**Fig. 7f**). Quartz-porphyry sills
505 that intrude and are interpreted as coeval with the King stratigraphy (**Fig. 6c**; labelled 1) are
506 intermediate to dacitic in composition (**Fig. 10c, d**), with high calc-alkaline Zr/Y (16.7-18.5)
507 and Th/Yb ratios, and low HFSE concentrations (**Fig. 10e-f**). Chondrite normalized REE
508 profiles are steep, both with respect to the LREE and HREE (**Fig. 11a**). The younger quartz-
509 porphyry sills (**Fig. 6c**, labelled 2) and late basaltic dykes were not analysed.

510 **6.3. Mobile element geochemistry**

511 The mobile element geochemistry of the King deposit is illustrated in **Figures 12 and 13**.
512 Regional metamorphism at King can be considered isochemical at the hand-specimen scale.
513 Although dewatering reactions during regional metamorphism may lead to the mobility of
514 volatile species (e.g. H_2S, F, CO_2; Spry, 2000; Corriveau & Spry, 2014), mobile element
515 characteristics will primarily reflect hydrothermal alteration prior to metamorphism (detailed
516 in Bonnet & Corriveau, 2007; Corriveau & Spry, 2014). Mass change values were not
517 calculated for samples from King as a suitable least altered precursor was not identified.
518 Weakly altered rocks analysed from Erayinia NW (eastern Murrin Domain) have distinct
519 immobile element characteristics (Hollis et al. in prep.) and are therefore not suitable for mass
520 change calculations at King, whereas those from King North are similarly altered to the rocks
521 described here (Kelly, 2018, unpublished thesis).

522 Garnet-amphibolites from the deep footwall of the King deposit are characterised by
523 high Fe_2O_{3T} (18-28 wt.%), and variable Cu (75-1315 ppm) and MgO (3-13 wt.%)
524 concentrations (**Figs. 12, 13**). This is consistent with varying degrees of Mg-metasomatism and
525 pyrrhotite-magnetite±chalcopyrite±pyrite mineralization in the feeder zone, stratigraphically
526 underlying massive sulfide mineralization (**Fig. 6d**; see Discussion). Calcium and SiO_2
527 concentrations are variable (39-51 wt.% SiO_2, 1-18 wt.% CaO) reflecting the abundance of
528 hornblende, epidote and quartz (**Fig. 12**). Sodium and K concentrations are low (<0.8 wt% for
529 each), consistent with a mafic protolith. Most pathfinder element concentrations are anomalous
530 (e.g. 2.8-15.1 ppm As, 0.3-4.2 ppm Sb) compared to unmineralized mafic rocks from the
531 Yilgarn Craton (Hollis et al., 2015), except for Tl, Bi and Au which are generally low (**Fig.**
532 **12**). Very high Mo (534 ppm) was noted in sample GK004 which is being targeted for Re-Os

geochronology. On the Box Plot of Large et al. (2001a) samples plot in both the 'least altered mafic' field and between the ankerite/dolomite and chlorite/pyrite mineral nodes reflecting variable enrichments in Ca, Fe and Mg.

Intermediate banded schists from the mixed footwall sequence show increased SiO_2 (58-76 wt.%) concentrations when compared to the stratigraphically underlying footwall garnet-amphibolites and have highly variable K_2O (0.3-1.4 wt.%) and Na_2O (0.7-2.7 wt.%) concentrations. This is consistent with the intense silicification in the mixed footwall sequence (**Fig. 6d**), together with a more evolved precursor composition (reflected by lower TiO_2 concentrations; **Fig. 13 -** EC056D), and varying albitic alteration. Significantly lower Fe_2O_{3T} (2.2-7.3 wt.%), MgO (2.8-7.4 wt.%), and Cu (3-58 ppm) reflect the decreased abundance of chlorite, sulfide and magnetite present in the drillcore (e.g. EC116D: **Fig. 13**). Lower Ag, As, Bi, Hg, Sb, and Alteration Index (A.I.) values in the intermediate rocks correlate with a decreased abundance of Zn (**Figs. 12, 13**). All samples analysed plot with the 'least altered andesite' field of the Box Plot (**Fig. 12**).

Quartz-muscovite schists in the immediate footwall to massive sulfides at King are characterized by the highest SiO_2 (72.5-93.4 wt.%) values measured, and variable Fe_2O_{3T} (0.5-6.7 wt.%) (**Fig. 12**). This reflects the intense silicification of host rocks and variable sulfide mineralization (pyrite±sphalerite). Low Na_2O (typically ~0.3 wt), MgO (0.2-1.0 wt.%) and CaO, correspond to lesser chloritic and albitic alteration, and Na-depletion though the sericitization of feldspar (subsequently recrystallized to coarse muscovite during prograde metamorphism). Element concentrations may have also been reduced through large mass gains of SiO_2. Sample GK044 (**Fig. 6c**) shows significantly higher concentrations of Na_2O, CaO (4.3 wt.%), MgO (2.5 wt.%), and lower SiO_2 (59.8 wt.%). This sample is a coherent, weakly altered dacite surrounded by sheared and intensely silica-sericite altered dacite. It most likely represents a coherent lava flow or a high-level intrusion that is interbedded with volcaniclastic rocks of similar composition. Hydrothermal fluids would have been preferentially focused through the latter. Only sample GK044 plots within the 'least altered dacite' field of the Box Plot with other samples trending towards the chlorite/pyrite and sericite mineral nodes (**Fig. 12**). Pathfinder elements vary in abundance in the quartz-muscovite schists, but are often high (to 72ppm Cd, 465 ppm Pb, 35 ppm Sb, >25 ppm Hg) compared to all other lithologies except massive sulfides (**Figs. 12, 13;** see following). Downhole concentrations of Ni and MnO correlate well with increased amounts of Fe and base metals (Zn+Pb) in the core (EC031D: **Fig. 13**). Arsenic concentrations increase systematically towards massive sulfides in the top ~10m of quartz-muscovite schist in hole EC031D, with corresponding increases in Ag, Au, Sb, Tl and positive Eu anomalies (Eu/Eu*; **Fig. 13**).

Three samples of massive sulfide were analysed from the King deposit (holes EC116D and EC113D). These rocks are characterized by high Fe_2O_{3T} (24-27 wt.%) and variable Zn (0.4-15.9 wt.%), reflecting the abundance of pyrrhotite, pyrite and sphalerite (**Figs. 12, 13**). Pathfinder concentrations of the following elements are anomalous to moderately high: Ag (28-50 ppm), As (40->250 ppm), Bi (2-52 ppm), Cd (95-452 ppm), Hg (>23 ppm), In (3-20 ppm), Te (4-10 ppm), Sb (6->250 ppm), and Se (5-25 ppm). Lead, Cu and Au concentrations are low (0.46-0.93 wt.% Pb, <125 ppm Cu, <0.1 g/t Au) compared to other VHMS deposits in the

Eastern Goldfields (Hollis et al. 2015). All samples display prominent positive Eu anomalies (**Fig. 11c**). Although Sn data is considered unreliable here due to poor accuracy and precision, massive sulfides have concentrations (27-112 ppm) well in excess of all other rocks analysed from the King deposit (typically ~2 ppm).

Hanging-wall strata (both banded schists and coherent amphibolites) are characterized by low SiO_2 (<57.2 wt.%). Concentrations of K_2O (0.7-1.7 wt.%), Na_2O (0.03-2.74 wt.%), MgO (1.5-7.8 wt.%) and CaO (0.8-7.9 wt.%) are variable (**Fig. 12**). Iron concentrations are high (11-24 wt.% Fe_2O_{3T}) reflecting the presence of abundant disseminated magnetite (with corresponding high magnetic susceptibility) and stringer pyrite (**Fig. 13**). Thallium and Sb concentrations are moderately high and similar to the quartz-muscovite schists adjacent to massive sulfides. All samples analysed plot near the ankerite/dolomite mineral node of the Box Plot due to very high CCPI, but moderate A.I. (~50%; **Fig. 12**). High CCPI is predominantly due to the abundance of Fe, with local carbonate-alteration (**Fig. 9p-r**). Pathfinder concentrations are typically low, except sample GK027 (with abundant stringer pyrite) that contains high As (167 ppm) and Se (7.6 ppm). This sample displays the most prominent positive Eu anomaly from those analysed in the hanging-wall of the King deposit (**Fig. 11b**).

7. Discussion

All the available evidence obtained to date is consistent with the King Zn deposit and its stratigraphy representing a metamorphosed and overturned VHMS system. This model is in agreement with the nature of the host rocks, grade and tonnage of the deposit, styles of mineralization, the observed mineralogy of the host sequence, and its geochemical characteristics. Each are discussed in turn. Finally, we discuss potential halos that may be used to find VHMS deposits in amphibolite facies greenstone belts of the Yilgarn Craton.

7.1. Volcanic environment

Although the host stratigraphy of the King deposit has been metamorphosed to amphibolite facies and is strongly deformed (e.g. **Fig. 7e-f**), its geological features are consistent with an evolving volcanic sequence deposited in a deep-marine, rifted-arc or more likely cratonic-rift setting. Immobile element geochemistry highlights an evolution of the footwall sequence from calc-alkaline basaltic magmatism with high Co and Ti concentrations, to andesitic and dacitic rocks (**Figs. 10, 13**) capped by massive sulfides. The return of thin mafic lithologies in the hanging-wall of similar composition to the footwall (**Figs. 10, 11**) is consistent with a shift in the geodynamic environment, possibly related to further extension (Piercey, 2011). This cyclicity has been noted from many VHMS camps worldwide, with mineralization occurring towards the end of a mafic to felsic eruptive cycle (Galley et al. 2007). It is difficult to determine if the volcanic sequence is dominated by flow or volcaniclastic units. However, recrystallised quartz clasts in the some of the mixed footwall sequence, along with the broad and diffuse alteration halo associated with VHMS mineralization at King favour the latter interpretation (after Gibson & Galley, 2007).

The presence of sulfide bearing graphitic schists at several stratigraphic horizons, including the ore horizon (drillhole EC116D), are indicative of a deep marine euxinic

environment, below storm wave base, for the entire stratigraphy. This setting would have provided a favourable chemical environment for the preservation of massive sulfides if formed on the paleoseafloor. By contrast, if mineralization formed through subseafloor replacive processes, fine-grained sediments may have acted to seal the hydrothermal system (Franklin et al. 2005). Due to the extensive recrystallization of primary textures, it is unclear whether the King deposit formed on the seafloor, or through replacive processes. The thin, sheet-like morphology of massive sulfide mineralization may suggest mineralization preferentially replaced a thin stratigraphic horizon, possibly of fine-grained graphitic sediments near the top of the quartz-muscovite schists (as appears to be the case in EC116D; **Fig. 9l**). The presence of minor sulfide mineralization (**Fig. 8g**) and the enrichment of pathfinder elements (e.g. Tl, Sb) in the immediate hanging-wall (**Fig.12**) could be consistent with either a replacive model, or seafloor exhalation if hydrothermal activity continued after the deposition of hanging-wall strata. Further evidence for a replacive model is the presence of milled rock fragments within massive sulfides (**Figs. 8e,i**). If massive sulfide mineralization formed predominantly through replacive processes, these clasts may represent remnants of the unreplaced host stratigraphy that were subsequently deformed during metamorphism and shearing.

The tectonic setting of the King stratigraphy, must be considered with regards to the wider 'arc vs plume' debate for the origin of the Eastern Goldfields (Czarnota et al. 2010; Barnes et al. 2012; Barnes & Van Kranendonk, 2014; Hollis et al. 2015, 2017a). The arc scenario, used to interpret the geochemistry of rock types present in the Eastern Goldfields Terrane (EGS), does not explain evidence for a common history between the Youanmi Terrane and EGS, which includes: (i) contemporaneous magmatism across the EGS and Youanmi Terrane from at least c. 2.82 Ga (Ivanic et al. 2010; Barnes et al. 2012); (ii) simultaneous inferred 'subduction-related' magmatism across the whole of the craton, which is inconsistent with the geometry of modern arc systems (Van Kranendonk et al. 2013); and (iii) stratigraphic similarities between the Kalgoorlie and Yamarna terranes, and Youanmi and Burtville terranes (Pawley et al. 2012). Furthermore, recent work has also demonstrated that mafic to felsic rocks of the EGS are geochemically consistent with the fractionation of plume-related tholeiitic basalts, coupled with their contamination by contemporaneous partial melts of pre-existing continental crust (Barnes et al. 2012; Barnes & Van Kranendonk, 2014; Hayman et al. 2015b). An arc is therefore not required.

Whole rock geochemical data from King are shown on the Th/Yb vs Nb/Yb plot of Pearce (2008) in **Figure 10g**. The geochemical trend away from the mantle array to higher Th/Yb ratios at King, favours the fractionation and crustal contamination of plume-derived basaltic magmas, rather than subduction related magmatism (which would parallel the mantle array; see Bédard et al. 2013). This trend is also apparent in samples analysed from Erayinia NW (~4km NW of King in the Murrin Domain; Hollis et al. in prep.) and at King North (Kelly, 2018, unpublished thesis). Magmatic activity inferred to be plume-related precedes all episodes of VHMS mineralization in the Younami Terrane (at c. 2.9 Ga, 2815 Ma, 2750 Ma and 2720 Ma; see Hollis et al. 2015). This plume-related activity is reflected by the repeated occurrence of komatiitic or high-Mg basaltic magmatism in the Youanmi Terrane, followed by the eruption and emplacement of major extrusive/intrusive mafic suites, terminated by felsic volcanism (van

Kranendonk et al. 2013; Ivanic et al. 2010) that hosts VHMS deposits (reviewed in Hollis et al. 2015, 2017b). Although the age of the King deposit is not clear, the presence of komatiite and BIF in the local area (see Regional Geology of Erayinia) may suggest it is of similar age to the Nimbus and Anaconda deposits of the Eastern Goldfields (~2705 Ma; Hollis et al., 2015, 2017b).

7.2. Deposit type, style, grade and tonnage

There are over 800 significant (>0.2 Mt) VHMS deposits worldwide, mostly of small tonnage (Galley et al. 2007; Piercey et al. 2015). Metal ratios reflect the tectonic setting at the time of mineralization, as metals are derived through the leaching of underlying strata with magmatic inputs in arc/backarc environments (Franklin et al. 2005; Galley et al. 2007; Piercey, 2011). Deposits may be classified as Cyprus-, Besshi-, Noranda-, Kuroko- and Bathurst-types, corresponding to the nature of their host rock sequences and dominant metals (i.e. mafic Cu-Zn, mafic-siliciclastic Cu-(Co-Zn-Ni), bimodal mafic Cu-Zn-Pb-(Ag-Au), bimodal-felsic Zn-Pb-Cu-(Au-Ag), and felsic-siliciclastic Zn-Pb-Cu-(Au-Ag) groups respectively; Franklin et al. 2005; Piercey, 2011). A sixth VHMS type (i.e. Eskay Creek-type), rich in precious metals, reflects hybrid deposits with both VHMS and shallow water epithermal characteristics (Piercey, 2011).

Equivalents to most of these VHMS types are present in the Yilgarn Craton. The Teutonic Bore, Jaguar and Bentley deposits of the Kambalda Terrane (**Fig. 1**) occur in mafic dominated volcanic sequences, with felsic volcanic complexes and deep-marine argillaceous sedimentary rocks near the ore horizon (Hallberg & Thompson, 1985; Belford et al. 2015). Although these deposits are relatively small (1.6 to 3.05 Mt), Zn grades are high (9.8 to 11.3%) and significant amounts of Cu are present (2 to 3.5%) with minor Pb (~0.6%). The Teutonic Bore deposits therefore closely resemble bimodal-mafic or Noranda-type deposits worldwide (median 3.0 Mt at 5.2% Zn, 1.7% Cu, 0.9% Pb: Piercey et al. 2015). Bimodal-felsic or Kuroko-type deposits are typically characterised by significantly higher Pb (~1.9%) and lower Cu (~1.4%) concentrations (Piercey et al. 2015; Yeats et al. 2017), but are more common in Palaeozoic volcanic sequences than the Archean (Huston et al. 2010). Examples of felsic-siliciclastic and hybrid-epithermal deposits in the Yilgarn Craton include the Hollandaire (Hayman et al. 2015a) and Nimbus deposits (Hollis et al. 2017a).

The current King deposit resource (2.15 Mt at 3.47% Zn), while significantly smaller than VHMS deposits in the Golden Grove camp of the Youanmi Terrane (e.g. Scuddles 10.5 Mt; **Fig. 1**), is of comparable size to most other resources in the Yilgarn Craton (e.g. Teutonic Bore 1.68 Mt, Just Desserts 1.07 Mt, Hollandaire 2.8 Mt; Austin 1.48 Mt, Manindi 1.35 Mt; see Hollis et al. 2015). The largest deposits in the Yilgarn often comprise multiple stacked lenses of massive sulfides (e.g. Gossan Hill: Sharpe & Gemmell, 2001; Nimbus: Hollis et al. 2017a). The King deposit is classified as a metamorphosed bimodal-mafic or Noranda-type VHMS deposit, due to the abundance of mafic to felsic volcanic rocks, low volume of siliciclastic rocks, low Pb concentrations in massive sulfides (0.47-0.93%), and presence of significant chalcopyrite in the feeder zone.

Within VHMS deposits worldwide a common metal zonation is often observed. In bimodal-mafic deposits, feeder systems are typically dominated by Cu and Fe sulfides, primarily chalcopyrite, pyrite and/or pyrrhotite (Galley et al. 2007). Overlying lenses of massive sulfides become increasingly pyrite-sphalerite±(galena) rich and pyrrhotite-chalcopyrite poor towards the paleo-seafloor (Galley et al. 2007). Gold and Ag may be associated with Cu-rich, Zn-rich mineralization, or both (Gibson & Galley, 2007), as appears to be the case at King (**Fig. 13**). Despite the extensive recrystallization of sulfide assemblages at King, the zonation from a pyrite-sphalerite rich lens of massive sulfide, stratigraphically underlain by a chloritic stockwork with abundant chalcopyrite, pyrrhotite and magnetite (**Fig. 6c**), is consistent with Noranda-type deposits if the local stratigraphy has been overturned. No resource is available for Cu and Au, due to the limited assaying for Au in massive sulfides, and both metals in the chloritic feeder zone. Samples analysed in this study reached 0.2 g/t Au in footwall rocks and 0.1 g/t Au in massive sulfides (**Sup. Table 1**). Historic intercepts include 5m at 0.6 g/t Au (drillhole EC046D) and 5.9m at 0.3g/t Au (EC031D). Copper concentrations reached 0.13% in lithogeochemistry samples (in the garnet-amphibolite), with corrected pXRF spot analyses reaching a maximum of 0.7%.

7.3. A metamorphosed hydrothermal system

Primary alteration minerals surrounding VHMS deposits include chlorite, sericite, carbonate, quartz and pyrite, with talc, epidote, albite and kaolinite (or sometimes other clay minerals) often present (Barrett et al. 2005; Galley et al. 2007; Yeats et al. 2017). In upper greenschist- to amphibolite-facies metamorphic terranes, distinctive coarse grained mineral suites commonly define VHMS alteration zones (Galley et al. 2007; Dusel-Bacon, 2012). These minerals can include, but are not limited to: chloritoid, garnet, staurolite, kyanite, andalusite, phlogopite, and gahnite (zincian spinel). The presence or absence of each of these minerals not only reflect VHMS style hydrothermal alteration and P-T conditions during metamorphism, but also the thermal gradient during metamorphism (Dusel-Bacon, 2012). A comprehensive list of metamorphosed VHMS deposits under different conditions (e.g. greenschist, granulite, blueschist), and common minerals associated with each, was given by Corriveau and Spry (2014).

Hydrothermal alteration at King is dominated by quartz-muscovite±chlorite±albite±carbonate in felsic to intermediate banded schists, and quartz–epidote±chlorite±magnetite in garnet-amphibolite. Cordierite and anthophyllite also occur in relatively minor amounts (≦5%) in felsic to intermediate footwall rocks. According to Corriveau and Spry (2014), the *"best documented alteration types associated with metamorphosed VHMS deposits are the cordierite-anthophyllite schists, commonly the amphibolite facies analogues of chloritic alteration pipes"* (p.181). Their distinct lithogeochemical signature (+Mg, +Fe, -Ca, -Na, -K) results in mineral assemblages that may include cordierite, orthoamphibole/orthopyroxene, Al_2SiO_5 polymorphs, garnet, or staurolite, quartz, biotite, and plagioclase, depending on P-T conditions. The aluminous minerals garnet, chloritoid, staurolite and the Al_2SiO_5 polymorphs (=andalusite, kyanite, sillimanite) commonly occur close to high-T alteration pipes. This reflects the enrichment of Al by leaching of alkalis

under high fluid/rock ratios (Dusel-Bacon, 2012). Metamorphosed phyllic, sericitic, and argillic alteration zones (+K, +Mg, ±Fe, -Ca, -Na) will result in the formation of diagnostic peraluminous and/or mica-rich metamorphic rocks (e.g. those unusually rich in Al_2SiO_5 polymorphs, cordierite, garnet, K-feldspars, and/or micas) (Corriveau & Spry, 2014).

At King, the abundance of silica-epidote in the footwall garnet-amphibolites is consistent with typical seafloor alteration of basaltic rocks prior to metamorphism (Galley et al. 2007). Prograde metamorphism of an Al-rich assemblage of basaltic rocks is also recorded by the presence of abundant garnet, with hornblende and biotite. Garnet can locally form up to 50% of the rock (**Fig. 7a** – upper core), which has often retrogressed to chlorite and quartz. The Cu-Fe sulfide bearing zone rich in chlorite and magnetite within the footwall garnet-amphibolites is consistent with a stockwork zone that often underlie lenses of massive sulfides that has been metamorphosed (Galley et al. 2007). The LREE variation in these footwall rocks has also been observed in intensely chlorite-altered stockwork zones elsewhere (e.g. Barrett & MacLean, 1994).

In overlying intermediate and felsic rocks the presence of significant Mg-rich cordierite and anthophyllite may also be taken as evidence for Mg-metasomatism prior to metamorphism (Barrett et al. 2005; Corriveau & Spry, 2014). Anthophyllite and cordierite are present within other metamorphosed VHMS footwall rocks of the Yilgarn Craton. Anthophyllite has been identified from the Just Desserts deposit (1.07 Mt at 1.82% Cu; Hassan, 2014), and in the Quinns district associated with the Austin deposit (1.48 Mt at 1.39% Zn, 1.02% Cu; Duuring et al. 2016). Cordierite-rich rocks have been identified associated with VHMS mineralization at Ravensthorpe (Witt, 1999), and Mount Gibson (Yeats & Groves, 1998).

The transition from chloritic and albitic alteration in intermediate lithologies to quartz-muscovite alteration in the overlying dacitic rocks (with lower TiO_2 – **Fig. 13**) reflects increased sericitization (+K, -Na, -Ca, -Mg) towards mineralization in footwall rocks prior to metamorphism. The intermediate rocks analysed here are generally only weakly altered (**Fig. 12** – see Box Plot). In the footwall quartz-muscovite schists, prograde metamorphism led to the recrystallization of an assemblage most likely dominated by quartz-sericite±pyrite ±(chlorite). These rocks are now dominated by fine granoblastic quartz with interstitial platy muscovite. Minor epidote, garnet and hornblende became sinks for Ca, Al, Fe, Mg and Na. Subsequent retrograde metamorphism is recorded by the replacement of the coarse muscovite by sericite and Mg-chlorite, sericitisation of cordierite, and breakdown of garnet to chlorite and quartz.

Most VHMS deposits worldwide metamorphosed to amphibolite facies are characterized by at least one Al-rich phase (Araujo et al. 1995). As stated previously, alteration assemblages containing Al-rich mineral phases are interpreted to represent the removal of SiO_2 and alkali elements by acidic fluids, and the residual concentration of Al_2O_3 in footwall rocks prior to metamorphism (Galley et al. 2007; Duuring et al. 2016). Staurolite porphyroblasts have been recognized surrounding the Hollandaire deposit with garnet (Hayman et al. 2015a), and at Wheatley with garnet, sillimanite and kyanite (Yeats, 2007; Hassan, 2017a) (**Fig. 1**). Andalusite has been identified in metamorphosed sedimentary and felsic rocks from the

Dalgaranga greenstone belt (Superior Zn prospect; Butt & Sergeev, 2003), in altered footwall rocks at Teutonic Bore (albeit in minor amounts; Hallberg & Thompson, 1985), at Hollandaire (with kyanite; Hayman et al. 2015a), and the Quinns district (with kyanite; Tasman and Franklin prospects: Duuring et al. 2017; Hassan, 2017b) (**Fig. 1**). Minor andalusite was also reported by Sharpe & Gemmell (2001) from the stratabound chlorite-(carbonate) alteration enveloping massive magnetite and sulfide mineralization at Gossan Hill. More globally, the Archean Geco deposit of the Superior Province, Canada, is a well-studied example of a bimodal-mafic VHMS deposit metamorphosed to upper amphibolite facies. Ore hosting lithologies now comprise muscovite-quartz±sillimanite schist, interpreted as a metamorphosed sericitic alteration zone (Dusel-Bacon, 2012).

Research on the Kristineberg VHMS deposit of lower amphibolite facies from the Skellefte district, Sweden, has shown that very different secondary assemblages such as andalusite-quartz-muscovite and cordierite-chlorite-talc can both be produced from the same precursor (e.g. rhyolite); and conversely the same mineral assemblages can also be produced from different precursor rocks, such as a weakly altered andesite and strongly altered rhyolite (Barrett et al. 2005). The authors proposed a series of reactions to explain the observed mineralogy at Kristineberg (namely quartz, Mg-chlorite, muscovite, cordierite, phlogopite/biotite, andalusite and pyrite). The most significant reactions here are:

1. 280 chlorite + 131 quartz → 231 cordierite + 180 anthophyllite + water
2. 40 chlorite + 28 sericite + 9 quartz → 33 cordierite + 32 phlogopite + 12 andalusite + 16 water
3. 140 chlorite + 49 sericite + 51 quartz → 141 cordierite + 56 phlogopite + 30 anthophyllite + water

The numbers before mineral names give the Niggli cation amounts of each mineral involved in the reactions. Note that the major difference between the second and third equations is the proportion of chlorite. When this is higher (eq. 3), cordierite, phlogopite/biotite, and anthophyllite may be produced without andalusite (Barrett et al. 2005). This may explain the prevalence of cordierite and anthophyllite (plus biotite) at King. Although we cannot rule out the presence of an Al_2SiO_5 phase, none were observed in thin section or under SEM.

7.4. Prospectivity of felsic rocks

The immobile element geochemistry of felsic volcanic rocks has long been used to distinguish VHMS fertile from unprospective camps (Lesher et al. 1986; Hart et al. 2004; Piercey, 2011). Quartz-muscovite schists of dacitic composition from King display similar geochemical characteristics to felsic rocks associated with VHMS deposits throughout the Yilgarn Craton (Hollis et al. 2015, 2017a), but with subtle differences. VHMS associated felsic rocks throughout the Yilgarn are characterized by: i) high SiO_2 in unaltered rocks; ii) tholeiitic to transitional Zr/Y and La/Yb values (i.e. FII to FIII affinity: **Fig. 14b**); iii) flattish REE profiles (La/Sm_{CN} <3, Dy/Yb_{CN} ~1); iv) high HFSE concentrations; v) high Sc/TiO_2 and Sc/V ratios; and low Th/Yb ratios (<2) (Hollis et al. 2015, 2017a). These felsic rocks are also equivalent to those which host VHMS deposits of the Pilbara Craton of Australia (Vearncombe & Kerrich, 1999) and the Abitibi greenstone belt of Canada (Barrie et al. 1993; **Fig. 14a**). One exception is the Nimbus Ag-Zn-(Au) deposit, near Kalgoorlie, which is hosted by FI affinity calc-alkaline dacite (**Figs. 11f, 14b**; Hollis et al. 2017b). Precious metal rich VHMS deposits

(i.e. Eskay Creek-type deposits) typically form at shallower water depths to classic Zn-Cu deposits and are often hosted by 'less prospective' FI- to FII-affinity, calc-alkaline rocks (Mercier-Langevin et al. 2011; **Fig. 14a**).

Although quartz-muscovite schists from King, display similar Zr/Y (4.6-15.0) and La/Sm ratios to felsic rocks from Teutonic Bore, HFSE concentrations are significantly lower (**Fig. 10e-f;** e.g. 68-236 ppm Zr) and HREE profiles are slightly steeper (**Fig. 11f**). While the HFSE depletion in the King felsic rocks may be a function of element dilution through mass gain, this would not explain higher Dy/Yb ratios. The FI (to FII) characteristics at King (**Fig. 10e-f**) might suggest reduced base metal prospectivity for the immediate area, in keeping with lower grades of Zn mineralization and abundant occurrences of massive Fe-sulfides. However, the geochemistry of felsic rocks further into the hanging-wall or footwall of the stratigraphy has not been tested. Furthermore, at King North (**Fig. 4**) recent geochemical work on rock chips from RC drilling (Kelly, 2018, unpublished thesis) has highlighted both FII and FIII affinity felsic rocks in close proximity to Cu-Zn-Au mineralization.

7.5. Vectors and halos to mineralization

Many vectors and halos have been proposed to help locate VHMS deposits in volcanic terranes subject to greenschist facies metamorphism. These are most powerful when used in combination, and include: i) changes in the mineralogy and chemistry of host sequence associated with the formation of quartz, chlorite, carbonate and sericite and the breakdown of feldspar and volcanic glass (e.g. Na_2O depletion); ii) elevated concentrations of pathfinder elements (e.g. Bi, Tl, Sb: Large et al. 2001b); iii) several alteration indices (e.g. Ishikawa, Silicification, CCPI); and iv) changes in chlorite, carbonate and white mica chemistry (Duuring et al. 2016).

Regarding alteration mineralogy, we have already described common minerals associated with metamorphosed VHMS systems. Recognition of mineral assemblages that include cordierite, anthophyllite, biotite/phlogopite, and/or abundant garnet would be significant in the Yilgarn Craton, in addition to Al-rich phases (i.e. kyanite, sillimanite, andalusite and/or staurolite) not present at King. In Ontario, Canada, mapping of the intensity and distribution of anthophyllite, cordierite, sillimanite, garnet, quartz, muscovite and staurolite led to the identification of footwall alteration and the discovery of the Archean bimodal-mafic Winston Lake deposit (Dusel-Bacon, 2012).

Zinc shows strong positive correlations with the following VHMS pathfinder elements at King: Ag, As, Au, Bi, Cd, Eu/Eu* (Eu anomaly), Hg, In, Ni, Pb, Sb, Se, Tl. Similar VHMS proximal metal enrichments of Ag, Au, Bi, Fe, In, MgO, Mo, S, Se and Te (with minor enrichments in As, Cd, Mn, and V) were noted from the Quinns VHMS region by Duuring et al. (2017). Thallium and Sb concentrations are moderately high and similar to quartz-muscovite schists immediately underlying massive sulfides (**Fig. 12**) and are comparable to other Australian VHMS systems which display well developed halos (Large et al. 2001b). Both elements show a progressive increase in abundance from the deep footwall garnet-amphibolites, through the mixed footwall sequence, quartz-muscovite schists, peaking in

862 massive sulfides and decreasing again in hanging-wall strata (**Fig. 12** – Box and Whisker
863 diagrams). Although negative Eu anomalies may have been originally present as a primary
864 feature of the felsic volcanic rocks due to plagioclase fractionation, Eu is readily liberated
865 during hydrothermal alteration associated with the breakdown of feldspar at temperatures
866 >250°C (Sverjensky, 1984). This leads to prominent positive Eu anomalies in hydrothermally
867 altered and mineralized volcanic rocks, as observed at King (**Fig. 11**), Nimbus (Hollis et al.
868 2017), and other VHMS deposits in the Yilgarn (Hollis et al., 2015).

869 Chemographic ternary diagrams are useful for portraying common alteration trends in
870 metamorphosed terranes, as shown in **Figure 15** (Bonnet & Corriveau, 2007; Corriveau &
871 Spry, 2014). Whereas samples of footwall garnet-amphibolite from the King deposit plot
872 towards the garnet, chlorite and hornblende mineral nodes, samples of quartz-muscovite schist
873 plot towards the cordierite node and A' corner (i.e. Al-rich end) of the diagram (**Fig. 15a**). The
874 prior is interpreted to reflect the intense Mg-Fe metamomatism of the feeder zone, and the latter
875 both quartz±sericite±pyrite alteration and Al-enrichment through alkali leaching of felsic
876 volcanic rocks prior to metamorphism. Weakly altered samples from the mixed footwall
877 sequence and intrusive quartz-feldspar porphyries plot closer to the least altered volcanic field.
878 Data from the Teutonic Bore and Wheatley deposits are also shown for comparison (**Figs.**
879 **15b,c**). The intensity of Fe and Mg enrichment at Teutonic Bore is highlighted by the strong
880 clustering of both mafic and felsic footwall strata between cordierite and garnet. At Wheatley,
881 mineralized felsic gneisses plot towards the cordierite mineral nodes, whereas hanging-wall
882 amphibolites are weakly altered.
883
884 In metamorphosed terranes, the Mn contents of ferromagnesian minerals such as garnet,
885 biotite, staurolite, chlorite and amphibole have been observed to increase with proximity to
886 sulfide deposits, as well as the Zn content of staurolite and spinel (i.e. gahnite) (Spry, 2000;
887 Corriveau & Spry, 2014). The pink colour of garnets at King suggest they are Mn-rich (i.e.
888 spessartine). MnO concentrations in the King footwall garnet-amphibolite reach 1.3wt% in
889 sample GK021. Large Mn peaks were also identified in garnet EDS spectra. Spessartine garnet
890 porphyroblasts have been observed in hanging-wall and footwall strata surrounding VHMS
891 mineralization in the Yilgarn Craton at Hollandaire and Wheatley (Hayman et al. 2015; Hassan,
892 2017a). Elevated contents of Mn in garnet from garnetites, and Zn in spinel from aluminous
893 gneisses were recently noted from granulite-facies rocks in the central Grenville Province,
894 Canada, highlighting its potential for VHMS mineralization (Hindemith et al. 2017). Corriveau
895 and Spry (2014) have further suggested that staurolite becomes increasingly orange with Zn
896 content. This may prove useful to identify further resources at Hollandaire and other regions
897 where staurolite porphyroblasts surround mineralization (Hayman et al. 2015a).
898
899 As regional metamorphism is largely an isochemical process at the core scale,
900 combinations of indices such as Ishikawa Alteration Index (A.I.), Carbonate-chlorite-pyrite
901 Index (CCPI; Large et al. 2001a), the Silicification Index ($100*SiO_2/SiO_2+Al_2O_3$) and the
902 ACNK Index ($Al_2O_3/CaO+Na_2O+K_2O$; Grunsky, 2013) may be used to discriminate between
903 different styles of footwall alteration and help locate mineralization. Alteration indices and
904 pathfinder elements are plotted against vertical distance to mineralization at King in **Figure**

905 **16**. Zinc and Fe concentrations are erratic in footwall rocks using both lithogeochemical and
906 pXRF datasets. Vanadium concentrations are highest in the feeder zone and may be useful to
907 identify such rocks elsewhere, particularly when combined with high A.I., ACNK Index values
908 and the abundance of normative corundum (see below). Antimony, Tl, In, and Eu/Eu* remain
909 low in both footwall and hanging-wall strata, only increasing significantly within short
910 distances (10s of metres) to mineralization. These are consequently only of use for exploration
911 when elevated. The ACNK Index and A.I. are high in both the chloritic zone and directly
912 underlying massive sulfides. The Silicification Index by contrast peaks in hanging-wall strata
913 directly overlying massive sulfides.
914
915 The abundance of calculated normative corundum was used by Grunsky (2013) for
916 rocks from the Abitibi greenstone belt, Canada. When Al is in excess over (Ca+Na+K), the
917 presence of normative corundum may be interpreted as extensive alkali leaching, a
918 characteristic feature of footwall alteration associated with VHMS deposits. At King,
919 normative corundum abundance is highest in the chloritic feeder zone, but importantly is not
920 present (i.e. >0) in any hanging-wall strata regardless of composition. This reflects the lack of
921 alkali-leaching in the hanging-wall and may be a useful tool to identify hydrothermal upflow
922 zones associated with VHMS deposits, and also hanging-wall from footwall sequences.
923 Normative quartz abundance generally parallels the Silicification Index trend, but drops in
924 weakly altered hanging-wall strata.
925
926 ## 8. Conclusions

927 The King Zn deposit (2.15 Mt at 3.47% Zn) occurs as a 2-5m thick stratiform lens
928 dominated by Fe sulfides, in a structurally overturned volcanic dominated sequence located
929 ~140km east of Kalgoorlie. The local stratigraphy is characterized by garnet amphibolite and
930 strongly banded intermediate to felsic schists with rare horizons of graphitic schist. Sulfide
931 mineralization is dominated by stratiform pyrite–pyrrhotite–sphalerite, with pyrite-(sphalerite)
932 and pyrrhotite–pyrite–(chalcopyrite) stringers at depth. The King deposit is classified as a
933 metamorphosed bimodal-mafic or Noranda-style VHMS deposit.

934 Footwall garnet-amphibolites are of sub-alkaline basaltic affinity, with high Co and Sc
935 concentrations, and flat chondrite-normalized HREE profiles. SiO_2, CaO, Fe_2O_{3T}, MgO and
936 Cu concentrations are highly variable, reflecting quartz–epidote±chlorite±magnetite±sulfide
937 alteration. Chlorite±magnetite alteration is most intense in the discordant Cu-bearing chloritic
938 feeder zone. Intermediate rocks are predominantly of calc-alkaline affinity and are similar to
939 andesites from elsewhere in the Kurnalpi terrane (e.g. Teutonic Bore). Although footwall
940 quartz-muscovite schists display similar Zr/Y and La/Sm ratios to felsic rocks from other
941 Archean VHMS deposits, HFSE concentrations are significantly lower and HREE profiles are
942 steeper. Hydrothermal alteration in felsic to intermediate rocks is characterized by a mineral
943 assemblage of quartz–muscovite±chlorite±albite±carbonate. Cordierite and anthophyllite are
944 locally significant and indicative of zones of Mg-metasomatism prior to metamorphism.
945 Increases of SiO_2, Fe_2O_{3T}, and depletions of Na_2O, CaO, and MgO occur in footwall quartz-
946 muscovite schists approaching massive sulfide mineralization.

Within all strata (including the immediate hanging-wall), the following pathfinder elements are strongly correlated with Zn: Ag, As, Au, Bi, Cd, Eu/Eu*, Hg, In, Ni, Pb, Sb, Se, Tl. These geochemical halos resemble less metamorphosed VHMS deposits across the Yilgarn Craton, and suggest that although metamorphism leads to element mobility and mineral segregation at the thin section scale, assay samples of ~20cm length are sufficient to vector to mineralization in amphibolite facies greenstone belts of the Eastern Goldfields. Recognition of minerals such as Mg-chlorite, muscovite, cordierite, anthophyllite, biotite/phlogopite, and abundant garnet are significant, in addition to Al-rich phases (kyanite, sillimanite, andalusite and/or staurolite) not present at King. Chemographic diagrams (e.g. A'KF and AFM) may be used to identify and distinguish different alteration trends, along with the following alteration indices: Ishikawa Alteration Index, Sericite Index, Silicification Index, ACNK Alteration Index, and the abundance of CIPW normative corundum and quartz.

Acknowledgements

This contribution builds upon the efforts of a large number of individuals, particularly ABM and CSA geologists. Chris Rosagro, David Mole and Jayson Meyers are thanked for thoughtful discussions on the geology of the Erayinia region. The principal author was supported by the Exploration Incentive Scheme at the Geological Survey of Western Australia, funded by the Western Australian Government Royalties for Regions Program. Whole rock geochemistry was funded by Black Raven Mining. Steven Hollis, Julian Menuge and Aileen Doran are supported by the Irish Centre for Research in Applied Geosciences (iCRAG). iCRAG is funded under the Science Foundation Ireland (SFI) Research Centres Programme (grant 13/RC/2092) and is co-funded under the European Regional Development Fund. Patrick Hayman and an anonymous reviewer are thanked for their constructive comments on this paper.

References

ABM Resources NL. (2008) Erayinia Project, Annual Report for the period ending 18th December, 2008. Unpublished report.

ABM Resources NL. (2009) Erayinia Project, Annual Report for the period ending 18th December, 2009. Unpublished report.

Araujo, S.M., Fawcett, J.J. & Scott, S.D. (1995) Metamorphism of hydrothermally altered volcanic rocks in a volcanogenic massive sulfide deposit: the Palmeiropolis, Brazil, example. *Revista Brasileira de Geociencias*, 25(3), 173-184.

Barley, M.E., Brown, S.J.A., Krapež, B. & Kositcin, N. (2008) Physical volcanology and geochemistry of a Late Archaean volcanic arc: Kurnalpi and Gindalbie Terranes, Eastern Goldfields Superterrane, Western Australia. *Precambrian Research,* 161, 53-76.

Barnes, S.J., Van Kranendonk, M.J. & Sonntag, I. (2012) Geochemistry and tectonic setting of basalts from the Eastern Goldfields Superterrane, Yilgarn Craton. *Australian Journal of Earth Sciences*, 59(5), 707-735.

Barnes, S.J. & Van Kranendonk, M.J. (2014) Archean andesites in the East Yilgarn Craton, Australia: products of plume/crust interaction? *Lithos*, 6, 80-92.

Barrett, T.J. & MacLean, W.H. (1994) Chemostratigraphy and hydrothermal alteration in exploration for VHMS deposits in greenstones and younger volcanic rocks. In: Lentz, D.R. (ed) Alteration and alteration processes associated with ore forming systems. *Geological Society of Canada Short Course Notes*, 11, 433-467.

990 Barrett, T.J., MacLean, W.H. & Arebäck, H. (2005) The Paleoproterozoic Kristineberg VMS deposit,
991 Skellefte district, northern Sweden. Part II: chemostratigraphy and alteration. *Mineralium Deposita*,
992 40, 368-395.
993 Bédard, J.H., Harris, L.B. & Thurston, P.C. (2013) The hunting of the snArc. *Precambrian Research*,
994 229, 20-48.
995 Belford, S.M., Davidson, G.J., McPhie, J. & Large, R.R. (2015) Architecture of the Neoarchean Jaguar
996 VHMS deposit, Western Australia: implications for prospectivity and presence of depositional
997 breaks. *Precambrian Research*, 260, 136-160.
998 Beresford, S., Stone, W.E., Cas, R., Lahaye, Y. & Jane, M. (2005) Volcanological controls on the
999 localization of the komatiite-hosted Ni-Cu-(PGE) Coronet Deposit, Kambalda, Western Australia.
1000 Economic Geology, 100, 1457-1467.
1001 Black, L.P., Kamo, S.L., Allen, C.M., Aleinikoff, J.N., Davis, D.W., Korsch, R.J. & Foudoulis, C.
1002 (2003) TEMORA 1: a new zircon standard for Phanerozoic U–Pb geochronology. *Chemical*
1003 *Geology*, 200, 155-170.
1004 Bonnet, A-L. & Corriveau, L. (2007) Alteration vectors to metamphosed hydrothermal systems in
1005 gneiss terranes. In: Goodfellow (ed) Mineral Deposits of Canada: a synthesis of major deposit-types,
1006 district metallogeny, the evolution of geological provinces, and exploration methods, p1035-1050.
1007 Boynton, W.V. (1984) Cosmochemistry of the rare earth elements: meteorite studies. In: Henderson
1008 (ed) Rare element geochemistry. Elsevier Pub. Co. Amsterdam, p63-114.
1009 Brown, S.J.A., Barley, M.E., Krapež, B. & Cas, R.A.F. (2002) The Late Archaean Melita Complex,
1010 Eastern Goldfields, Western Australia: shallow submarine bimodal volcanism in a rifted arc
1011 environment. *Journal of Volcanology and Geothermal Research*, 115, 303-327.
1012 Butt, C.R.M. & Sergeev, N.B. (2003) Dalgaranga base metal prospect, Mt. Magnet district, Western
1013 Australia. CRC Leme, CISRO Exploration and Mining, Bentley, Western Australia, 3p.
1014 http://crcleme.org.au/RegExpOre/Dalgaranga.pdf
1015 Cabanis, B. & Lecolle, M. (1989; in French) Le diagramme La/10-Y/15-Nb/8; un outil pour la
1016 discrimination des series volcaniques et la mise en evidence des procusses de melange et/ou de
1017 contamination crustale. The La/10-Y/15-Nb/8 diagram; a tool for distinguishing volcanic series and
1018 discovering crustal mixing and/or contamination. Comptes Rendus de l'Academie des Sciences,
1019 Serie 2, Mecanique, Physique, Chimie, Sciences de 1, Univers, Sciences de la Terre, 309, 2023-
1020 2029.
1021 Caruso, S., Fiorentini, M., Hollis, S.P., LaFlamme, C., Baumgartner, R.J., Steadman, J. & Savard, D.
1022 (in review) The fluid evolution of the Nimbus Ag-Zn-(Au) deposit: an interplay between mantle
1023 plume and microbial activity. *Precambrian Research.*
1024 Cassidy, K.F., Champion, D.C., Krapež, B., Barley, M.E., Brown, S.J.A., Blewett, R.S., Groenewald,
1025 P.B. & Tyler, I.M. (2006) A revised geological framework for the Yilgarn Craton, Western
1026 Australia. Western Australia Geological Survey, Record 2006/8: 8p.
1027 Champion, D.C. & Cassidy, K.F. (2000) Granites of the northern Eastern Goldfields: their distribution,
1028 age, geochemistry, petrogenesis, relationship with mineralisation, and implications for tectonic
1029 environment. In: Cassidy, K.F., Champion, D.C., McNaughton, N.J., Fletcher, I.R., Whitaker, A.J.,
1030 Bastrakova, I.V. & Budd, A.R., AMIRA P482 report—The Characterisation and Metallogenic
1031 Significance of Archaean Granitoids of the Yilgarn Craton (Chapter 2).
1032 http://www.doir.wa.gov.au/meriwa/reports/minexplor.PDF.
1033 Corriveau, L. & Spry, P.G. (2014) Metamorphosed hydrothermal ore deposits. In: Scott, SD. (ed)
1034 Treatsie on Geochemistry, Second Edition, p175-194. DOI: 10.1016/B978-0-08-095975-7.01107-4.
1035 Czarnota, K., Champion, D.C., Goscombe, B., Blewett, R.S., Cassidy, K.F., Henson, P.A. &
1036 Groenewald, P.B. (2010) Geodynamics of the eastern Yilgarn Craton. *Precambrian Research*, 183,
1037 175-202.

1038 Dusel-Bacon, C. (2012) Petrology of metamorphic rocks associated with volcanogenic massive sulfide
1039 deposits in volcanogenic massive sulfide occurrence model. U.S. Geological Survey Scientific
1040 Investigations Report 2010-5070-C, chap 17, 10p.
1041 Duuring, P., Hassan, L., Zelic, M. & Gessner, K. (2016) Geochemical and spectral footprint of
1042 metamorphosed and deformed VMS-style mineralization in the Quinns district, Yilgarn Craton,
1043 Western Australia. *Economic Geology*, 111, 1411-1438.
1044 Fisher, L., Gazley, M.F., Baensch, A., Barnes, S.J., Cleverly, J. & Duclaux, G. (2014) Resolution of
1045 geochemical and lithostratigraphic complexity: a workflow for application of portable X-ray
1046 fluoresence to mineral exploration. *Geochemistry: Environment, Exploration, Analysis*, 15, 113-124.
1047 Franklin, J.M., Gibson, H.L., Galley, A.G. & Jonasson, I.R. (2005) Volcanogenic massive sulfide
1048 deposits. In: Hedenquist, J., Thompson, J.F.H., Goldfarb, R.J. & Richards, J.P. (eds) Economic
1049 Geology 100th Anniversary Volume. Littleton, CO, Society of Economic Geologists, p523-560.
1050 Gazley, M.F. and Fisher, L. (2014) A review of the reliability and validity of portable X-ray
1051 fluorescence spectrometry (pXRF) data. Mineral Resource and Ore Reserve Estimation - The
1052 AusIMM Guide to Good Practice (2nd Ed), p.69-82.
1053 Galley, A.G., Hannington, M.D. & Jonasson, I.R. (2007) Volcanogenic massive sulfide deposits. In:
1054 Goodfellow, W.D. (ed). A synthesis of major deposit-types, district metallogeny, the evolution of
1055 geological provinces, and exploration methods. Geological Association of Canada, Mineral Deposits
1056 Division, Special Publication, 5, 141-161.
1057 Gee, R.D., Baxter, J.L., Wilde, S.A. & Williams, I.R. (1981) Crustal development in the Archaean
1058 Yilgarn Block, Western Australia, vol. 7. Geological Society of Australia, 43-56 (special
1059 publication).
1060 Gibson, H. & Galley, A. (2007) Volcanogenic massive sulphides of the Archean, Noranda District,
1061 Quebec. In: Goodfellow, W.D. (ed) Mineral Deposits of Canada: a synthesis of major deposit-types,
1062 district metallogeny, the evolution of geological provinces, and exploration methods. Special
1063 Publication No. 5, Mineral Deposits Division, Geological Association of Canada, p533-552.
1064 Green, D. & Schodlok, M. (2016) Characterisation of carbonate minerals from hyperspectral TIR
1065 scanning using features at 14 000 and 11 300nm. *Australian Journal of Earth Sicences,* 63, 951-957.
1066 Grunsky E.C. (2013) Predicting Archaean volcanogenic massive sulphide deposit potential from
1067 lithogeochemistry: application to the Abitibi Greenstone Belt. *Geochemistry: Exploration,*
1068 *Environment, Analysis*, 13, 317-336.
1069 Guilliamse, J.N. (2014) Assessing the potential for volcanic-associated massive sulfide mineralization
1070 at Weld Range, using Golden Grove for comparison. Geological Survey of Western Australia,
1071 Report 141, 61p.
1072 Hallberg, J.A. & Thompson, J.F.H. (1985) Geologic Setting of the Teutonic Bore, Massive Sulfide
1073 Deposit, Archean Yilgarn Block, Western Australia. *Economic Geology*, 80, 1953-1964.
1074 Hancock, E.A., Green, A.A., Huntington, J.F., Schodlok, M.C. & Whitbourne, L.B. (2013) Hylogger-
1075 3: implication of adding thermal-infrared sensing. Geological Survey of Western Australia, Record
1076 2013/3, 24p.
1077 Hannington, M.D., de Ronde, C.E.J. & Peterson, S. (2005) Sea-floor tectonics and submarine
1078 hydrothermal systems. *Economic Geology 100th Anniversary Volume*, 111-141.
1079 Hart, T.R., Gibson, H.L. & Lesher, C.M. (2004) Trace element geochemistry and petrogenesis of felsic
1080 volcanic rocks associated with volcanogenic massive Cu-Zn-Pb sulfide deposits. *Economic*
1081 *Geology*, 99, 1003-1013.
1082 Hassan, L.Y. (2014) The Yuinmery volcanogenic massive sulfide prospects: mineralization,
1083 metasomatism and geology. Geological Survey of Western Australia, Report 131,65p.
1084 Hassan, L.Y. (2017a) Metamorphosed VMS mineralization at Wheatley, southwest Western Australia.
1085 Geological Survey of Western Australia, Record 2017/9, 39p.

1086 Hassan, L.Y. (2017b) Alteration associated with the Austin-Quinns VMS prospects, northern Yilgarn
1087 Craton. Geological Survey of Western Australia, Record 2017/10, 61p.
1088 Hastie, A.R., Kerr, A.C., Pearce, J.A. & Mitchell, S.F. (2007) Classification of altered volcanic island
1089 arc rocks using immobile trace elements: development of the Th-Co discrimination diagram. *Journal*
1090 *of Petrology*, 48, 2341-2357.
1091 Hayman, P.C., Hull, S.E., Cas, R.A.F., Summerhayes, E., Amelin, Y., Ivanic, T. & Price, D. (2015a) A
1092 new period of volcanogenic massive sulfide formation in the Yilgarn: a volcanological study of the
1093 ca 2.76 Ma Hollandaire VMS deposit, Yilgarn Craton, Western Australia. *Australian Journal of*
1094 *Earth Sciences*, 62, 189-210.
1095 Hayman, P.C., Thébaud, N., Pawley, M.J., Barnes, S.J., Cas, R.A.F., Amelin, Y., Sapkota, J., Squire,
1096 R.J., Campbell, I.H. & Pegg. I. (2015b) Evolution of a ~2.7 Ga large igneous province: a
1097 volcanological, geochemical and geochronological study of the Agnew Greenstone Belt, and new
1098 regional correlations for the Kalgoorlie Terrane (Yilgarn Craton, Western Australia). *Precambrian*
1099 *Research*, 270, 334-368.
1100 Herrmann, W., Blake, M., Doyle, M., Huston, D., Kamprad, J., Merry, N. & Pontual, S. (2001) Short
1101 wavelength infrared (SWIR) spectral analysis of hydrothermal alteration zones associated with base
1102 metal sulfide deposits at Rosebery and Western Tharsis, Tasmania, and Highway-Reward,
1103 Queensland. *Economic Geology*, 96, 939-955.
1104 Hindemith, M., Indares, A. & Piercey, S.J. (2017) Hydrothermally altered volcanic rocks
1105 metamorphosed at granulite-facies conditions: an example from the Grenville Province. *Canadian*
1106 *Journal of Earth Sciences*, 54(6), 622-638.
1107 Hollis, S.P., Yeats, C.J., Wyche, S., Barnes, S.J., Ivanic, T.J., Belford, S.M., Davidson, G.J., Roache,
1108 A.J. & Wingate, M.T.D. (2015) A review of volcanic-hosted massive sulfide (VHMS)
1109 mineralization in the Archaean Yilgarn Craton, Western Australia: Tectonic, stratigraphic and
1110 geochemical associations. *Precambrian Research*, 260, 113-135.
1111 Hollis, S.P., Mole, D.R., Gillespie, P., Barnes, S.J., Tessalina, S., Cas, R.A.F., Hildrew, C., Pumphrey,
1112 A., Goodz, M.D., Caruso, S., Yeats, C.J., Verbeeten, A., Belford, S.M., Wyche, S. & Martin, L.A.J.
1113 (2017a) 2.7 Ga plume associated VHMS mineralization in the Eastern Goldfields Superterrane,
1114 Yilgarn Craton: insights from the low temperature and shallow water, Ag-Zn-(Au) Nimbus deposit.
1115 *Precambrian Research*, 291, 119-142.
1116 Hollis, S.P., Yeats, C.J., Wyche, S., Barnes, S.J. & Ivanic, T. (2017b) VHMS mineralization in the
1117 Yilgarn Craton, Western Australia: a review of known deposits and prospectivity analysis of felsic
1118 volcanic rocks. Geological Survey of Western Australia, Report, 165, 68p.
1119 Huston, D.L., Pehrsson, S., Eglington, B.M. & Zaw, K. (2010) The geology and metallogeny of
1120 volcanic-hosted massive sulfide deposits: variations through geologic time and with tectonic setting.
1121 *Economic Geology*, 105, 571-592.
1122 Huston, D.L., Champion, D.C. & Cassidy, K.F. (2014) Tectonic controls on the endowment of
1123 Neoarchean cratons in volcanic-hosted massive sulfide deposits: evidence from lead and neodymium
1124 isotopes. *Economic Geology*, 109, 11–26.
1125 Ishikawa, Y., Sawaguchi, T., Iwaya, S. & Horiuchi, M. (1976) Delineation of prospecting targets for
1126 Kuroko deposits based on modes of volcanism of underlying dacite and alteration haloes. *Mining*
1127 *Geology*, 26, 105-117.
1128 Ivanic, T.J., Wingate, M.T.D., Kirkland, C.L., Van Kranendonk, M.J. & Wyche, S. (2010) Age and
1129 significance of voluminous mafic-ultramafic magmatic events in the Murchison Domain, Yilgarn
1130 Craton. *Australian Journal of Earth Science*, 57, 597-614.
1131 Jenner, G.A. (1996) Trace element geochemistry of igneous rocks: geochemical nomenclature and
1132 analytical geochemistry. In: Wyman, D.A. (Ed.) *Trace Element Geochemistry of Volcanic Rocks:*

Applications for Massive Sulfide Exploration. Geological Association of Canada, Short Course Notes 12, 51-77.

Jiang, S-Y., Palmer, M.R. & Yeats, C.J. (2002) Chemical and boron isotopic compositions of tourmaline from the Archean Big Bell and Mount Gibson gold deposits, Murchison Province, Yilgarn Craton, Western Australia. *Chemical Geology*, 188, 229-247.

Jones, S.A. (2007) Geology of the Erayinia 1:100 000 sheet. Western Australia Geological Survey, 1:100 000 Geological Series Explanatory Notes, 37p.

Kelly, J. (2018) Characterisation of the King North Volcanic Massive Sulfide Deposit, Yilgarn Craton, Australia. Unpublished 4th year undergraduate thesis. University of Southampton, UK.

Krapež, B. & Hand, J.L. (2008). Late Archaean deep-marine volcaniclastic sedimentation in an arc-related basin: the Kalgoorlie Sequence of the Eastern Goldfields Superterrane, Yilgarn Craton, Western Australia. *Precambrian Research,* 161, 89-113.

Laakso, K., Peter, J.M., Rivard, B. & White, H.P. (2016) Short-wave infrared spectral and geochemical characteristics of hydrothermal alteration at the Archean Izok Lake Zn-Cu-Pb-Ag volcanogenic massive sulfide deposit, Nunavut, Canada: applications in exploration target vectoring. *Economic Geology*, 111, 1223-1239.

Large, R.R., Gemmell, J.B. & Paulick H. (2001a) The Alteration Box Plot: a simple approach to understanding the relationship between alteration mineralogy and lithogeochemistry associated with volcanic-hosted massive sulfide deposits. *Economic Geology*, 96, 957-971.

Large, R.R., McPhie, J., Gemmell, J.B., Herrmann, W. & Davidson, G.J. (2001b) The spectrum of ore deposit types, volcanic environments, alteration halos, and related exploration vectors in submarine volcanic successions: some examples from Australia. *Economic Geology*, 96, 913-938.

Lesher, C.M., Goodwin, A.M., Campbell, I.H. & Gorton, M.P. (1986) Trace-element geochemistry of ore-associated and barren, felsic metavolcanic rocks in the Superior province, Canada. *Canadian Journal of Earth Sciences*, 23, 222-237.

Le Valliant, M., Barnes, S.J., Fisher, L., Fiorentini, M.L. & Caruso, S. (2014) Use and calibration of portable X-ray fluorescence analysers: application to lithogeochemical exploration for komatiite-hosted nickel sulfide deposits. *Geochemistry: Exploration, Environment, Analysis*, 14, 199-209.

MacLean, W.H. (1990) Mass change calculations in altered rock series. *Mineralium Deposita*, 25, 44-49.

McConachy, T.F., McInnes, B.I.A. & Carr, G.R. (2004) Is Western Australia intrinsically impoverished in volcanogenic massive sulfide deposits or under explored? In: McConachy, T.F. & McInnes, B.I.A. (eds). Copper-zinc massive sulfide deposits in Western Australia. CSIRO Explores 2, 15-32.

McDonough, W.F. & Sun, S.S. (1995) The composition of the Earth. *Chemical Geology*, 120, 223-253.

McLeod, R.L., Gabell, A.R., Green, A.A. & Gadavski, V. (1987) Chlorite infrared spectral data as proximity indicators of volcanogenic massive sulfide mineralisation: Pacific Rim Congress 87, Gold Coast, Queensland, August 26, 1987, p321-324.

Mercier-Langevin, P., Hannington, M.D., Dubé, B. & Bécu, V. (2011) The gold content of volcanogenic massive sulfide deposits. *Mineralium Deposita*, 46, 509-539.

Mole, D.R., Fiorentini, M.L., Cassidy, K.F., Kirkland, C.L., Thebaud, N., McCuaig, T.C., Doublier, M.P., Duuring, P., Romano, S.S., Maas, R., Belousova, E.A., Barnes, S.J. & Miller, J. (2014) Crustal evolution, intra-cratonic architecture and the metallogeny of an Archaean craton. In: Jenkin, G.R.T., Lusty, P.A.J., Mcdonald, I., Smith, M.P., Boyce, A.J., Wilkinson, J.J. (eds) Ore Deposits in an Evolving Earth. Geological Society, London, p.393 (special publication).

Myers, J.S. (1990) Precambrian tectonic evolution of a part of Gondwana, southwestern Australia. *Geology*, 18, 537-540.

Nasdala, L., Hofmeister, W., Norberg, N., Martinson, J.M., Corfu, F., Dörr, W., Kamo, S.L., Kennedy, A.K., Kronz, A. & Reiners, P.W. (2008) Zircon M257-a Homogeneous Natural Reference Material

for the Ion Microprobe U-Pb Analysis of Zircon. *Geostandards and Geoanalytical Research*, 32, 247-265.

Nelson, D.R. (1995) 104973: metadacite porphyry, east of Liberty Bore. In: Compilation of SHRIMP U-Pb zircon geochronology data, 1994. Western Australia Geological Survey, Record 1995/3, 158-161.

Nelson, D.R. (1996) 104971: metatonalite, Round Hill. In: Compilation of SHRIMP U-Pb zircon geochronology data, 1995. Western Australia Geological Survey, Record 1996/5, 43-46.

Nelson, D.R. (1997) Evolution of the Archaean granite-greenstone terranes fo the Eastern Goldfields, Western Australia: SHRIMP U-Pb zircon constraints. *Precambrian Research*, 83, 57-81.

Pawley, M.J., Wingate, M.T.D., Kirkland, C.L., Wyche, S., Hall, C.E., Romano, S.S. & Doublier, P. (2012) Adding pieces to the puzzle: episodic crustal growth and a new terrane in the northeast Yilgarn Craton, Western Australia. *Australian Journal of Earth Sciences*, 59, 603-623.

Pearce, J.A. (1996) A user's guide to basalt discrimination diagrams. In: Wyman, D.A. (Ed.), *Trace Element Geochemistry of Volcanic Rocks: Applications for Massive Sulfide Exploration.* Geological Association of Canada, Short Course Notes 12, 79-113.

Pearce, J.A. (2014) Immobile element fingerprinting of ophiolites. *Elements*, 10, 101-108.

Pearce, J.A. & Cann, J.R. (1973) Tectonic setting of basic volcanic rocks determined using trace element analyses. *Earth and Planetary Science Letters*, 19, 290-300.

Piercey, S.P. (2011) The setting, style, and role of magmatism in the formation of volcanogenic massive sulfide deposits. *Mineralium Deposita*, 46, 449-471.

Piercey, S.P. & Devine, M.C. (2014) Analysis of powdered reference materials and samples by portable X-ray fluorescence spectrometer: performance and application to lithogeochemistry. *Geochemistry: Exploration, Environment, Analysis*, 14, 139-148.

Piercey, S.J., Paradis, S., Murphy, D.C. & Mortensen, J.K. (2001) Geochemistry and paleotectonic setting of felsic volcanic rocks in the Finlayson Lake, volcanic-hosted massive sulfide district, Yukon, Canada. *Economic Geology*, 96, 1877-1905.

Piercey, S.J., Peter, J.M. & Herrington, R.J. (2015) Zn-rich volcanogenic massive sulphide (VMS) deposits. In: Archibald, S.M. & Piercey, S.J. (eds) Current Perspectives on Zinc Deposits. Irish Association for Economic Geology, p37-57.

Podmore, D. & James, M. (2016) E28/1228. Extension of Term Application. Submitted to Department of Mines and Petroleum. Report Ref: R014.2016 E28/1228.

Rudnick, R.L. & Fountain, D.M. (1995) Nature and composition of the continental crust: a lower crustal perspective. *Review of Geophysics*, 33, 267-309.

Sharpe, R. & Gemmell, J.B. (2001) Alteration characteristics fo the Archean Golden Grove Formation at the Gossan Hill deposit, Western Australia: induration as a focusing mechanism for mineralizing hydrothermal fluids. *Economic Geology*, 96, 1239-1262.

Spry, P.G. (2010) Sulfidation and oxidation halos as guides in the exploration for metamorphosed massive sulfide deposits. *Reviewes in Economic Geology*, 11, 149-161.

Squire, R.J., Allen, C.M., Cas, R.A.F., Campbell, I.H., Blewett, R.S. & Enchain, A.A. (2010) Two cycles of voluminous pyroclastic volcanism and sedimentation related to episodic granite emplacement during the late Archean: Eastern Yilgarn Craton, Western Australia. *Precambrian Research*, 183, 251-274.

Sverjensky, D.A. (1984) Europium redox equilibria in aqueous solution. *Earth and Planetary Science Letters*, 67, 70-78.

Swager, C.P. (1995) Geology of the greenstone terranes in the Kurnalpi-Edjudina region, southeastern Yilgarn Craton: Western Australia Geological Survey, Report 47, 31p.

Swager, C.P. (1997) Tectono-stratigraphy of the late Archaean greenstone terranes in the southern Eastern Goldfields, Western Australia. *Precambrian Research*, 83, 11-42.

1229 Swager, C.P., Goleby, B.R., Drummond, B.J., Rattenbury, M.S. & Williams, P.R. (1997) Crustal
1230 structure of granite-greenstone terranes in the Eastern Goldfields, Yilgarn Craton, as revealed by
1231 seismic reflection profiling, *Precambrian Research*, 83, 43-56.
1232 Taylor, S.R. & Mclennan, S.M. (1985) The Continental Crust: its composition and evolution.
1233 Blackwell, Oxford.
1234 Van Kranendonk, M.J., Ivanic, T.J., Wingate, M.T.D., Kirkland, C.L. & Wyche, S. (2013) Long-lived,
1235 autochthonous development of the Archean Murchison Domain, and implications for Yilgarn Craton
1236 tectonics. *Precambrian Research*, 229, 49-92.
1237 van Ruitenbeek, F.J.A., Cudahy, T., van der Meer, F.D. & Hale, M. (2012) Characterization of the
1238 hydrothermal systems associated with Archean VMS-mineralization at Panorama, Western
1239 Australia, using hyperspectral, geochemical and geothermometric data. *Ore Geology Reviews*, 45,
1240 33-46.
1241 Vearncombe, S. (2010) Yilgarn volcanogenic massive sulfides. In: Wyche, S. (Ed.), Yilgarn-Superior
1242 Workshop – Abstracts, Fifth International Archean Symposium. Geological Survey of Western
1243 Australia, Record 2010/20, 47-50.
1244 Vearncombe, S. & Kerrich, R. (1999) Geochemistry and geodynamic setting of volcanic and plutonic
1245 rocks associated with Early Archaean volcanogenic massive sulfide mineralization, Pilbara Craton.
1246 *Precambrian Research*, 98, 243-270.
1247 Wagner, T., Klemd, R., Wenzel, T. & Mattsson, B. (2007) Gold upgrading in metamorphsoed massive
1248 sulfide ore deposits: direct evidence from laser-ablation-inductively coupled plasma-mass
1249 spectrometry analysis of invisible gold. *Geology*, 35(9), 775-778.
1250 Whitney, D.L. & Evans, B.W. (2010) Abbreviations for names of rock-forming minerals. *American*
1251 *Mineralogist*, 95, 185-187.
1252 Wingate, M.T.D. & Bodorkos, S. (2007a) 177916: metasiltstone, Karonie Mine; Geochronology dataset
1253 665. In: Compilation of geochronology daya. Western Australia Geological Survey.
1254 Wingate, M.T.D. & Bodorkos, S. (2007b) 177919: felsic metavolcanic rock, Urania Prospect;
1255 Geochronology dataset 666. In: Compilation of geochronology daya. Western Australia Geological
1256 Survey.
1257 Wingate, M.T.D., Kirkland, C.L. & Bodorkos, S. (2010) Introduction to geochronology data released
1258 in 2010. Geological Survey of Western Australia, Perth.
1259 Wingate, M.T.D., Lu, Y., Kirkland, C.L. & Spaggiari, C.V. (2016) 182419: granite gneiss, Coonana
1260 Hill, Geochronology Record 1300. Geological Survey of Western Australia, 4p.
1261 Witt, W.K. (1991) Regional metamorphic controls on alteration assemblages associated with gold
1262 mineralization in the Eastern Goldfields Province, Western Australia: implications for the timing
1263 and origin of Archaean lode-gold deposits. *Geology*, 19, 982-985.
1264 Witt, W.K. (1999) The Archaean Ravensthorpe Terrane, Western Australia: synvolcanic Cu-Au
1265 mineralization in a deformed island arc complex. *Precambrian Research*, 96, 143-181.
1266 Witt, W.K. & Hagemann, S. (2012) Syn-volcanic hydrothermal alteration in the Yilgarn Craton
1267 greenstones. CET Newsletter: 28-39.
1268 Wyche, S., Pawley, M.J., Chen, S.F., Ivanic, T.J., Zibra, I., Van Kranendonk, M.J., Spaggiari, C.V. &
1269 Wingate, M.T.D., (2013) Geology of the northern Yilgarn Craton. In: Wyche, S., Ivanic, T.J., Zibra,
1270 I. (Eds.) *Youanmi and southern Carnarvon seismic and magnetotelluric (MT) workshop.* Geological
1271 Survey of Western Australia. Record 2013/6, pp. 31-60.
1272 Yeats, C.J. (2007) VHMS mineral systems in the Yilgarn – characteristics and exploration potential. In:
1273 Bierlein, F.P. (Ed.) *Proceedings of Geoconferences (WA) Inc. Kalgoorlie 07 Conference*, 65–69.
1274 Yeats, C.J. & Groves, D.I. (1998) The Archaean Mount Gibson gold deposits, Yilgarn Craton, Western
1275 Australia: products of combined synvolcanic and syntectonic alteration and mineralisation. *Ore*
1276 *Geology Reviews*, 13, 103-129.

Yeats, C.J., Hollis, S.P., Halfpenny, A., Corona, J-C. LaFlamme, C., Southam, G., Fiorentini, M., Herrington, R.J. & Spratt, J. (2017) Actively forming Kuroko-type volcanic-hosted massive sulfide (VHMS) mineralization at Iheya North, Okinawa Trough, Japan. *Ore Geology Reviews*, 84, 20-41.

List of Figures

Figure 1. Major terrane and domain subdivisions of the Yilgarn Craton, Western Australia, showing the distribution of greenstone belts and base metal occurrences (red stars) (after Hollis et al. 2015). Significant VHMS deposits are labelled. *Domains:* B, Boorara; E, Edjudina; G, Gindalbie; L, Linden; Me, Menangina; Mu, Murrin. *Other abbreviations:* GB, greenstone belt; MB, metamorphic belt. The Teutonic Bore camp includes the Teutonic Bore, Jaguar and Bentley VHMS deposits.

Figure 2. Simplified stratigraphy of the Kalgoorlie and Kurnalpi terranes of the Eastern Goldfields (after Czarnota et al. 2010). Two main episodes of VHMS mineralization have been recognized (Hollis et al. 2015, 2017a): 1. ca. 2705 Ma: Anaconda (A), Nimbus (N), King?; 2. ca. 2690-2680 Ma: Teutonic Bore (TB), Jaguar, Bentley, Erayinia NW, Jungle Pool occurrence.

Figure 3. Regional Nd isotope variations of the Yilgarn Craton (modified after Wyche et al. 2013). The position of significant VHMS occurrences associated with the Kurnalpi paleo-rift zone (highlighted by younger depleted mantle model ages) are indicated by red stars.

Figure 4. Geological map of the central Erayinia region (modified after Jones, 2007), highlighting the position of the King deposit in the Edjudina Domain, east of the Claypan Fault.

Figure 5. Distribution of banded iron formations (BIF) and komatiites in the southern Eastern Goldfields Superterrane. The figure was derived from 2010 GSWA 1: 100 000 scale outcrop mapping, overlain on the domains of Cassidy et al. (2006). Also shown are U-Pb zircon age constraints from each domain, and the location of Ni-sulfide occurrences (from GeoVIEW; available at www.dmp.wa.gov.au).

Figure 6. (a) Drillhole map of the King Zn-(Cu) deposit. **(b)** Composite longitudinal section through the deposit highlighting the two Zn-rich ore lenses (after ABM Resources NL, Annual Report 2009). Zinc **(c)** Cross section showing the interpreted main geological units discussed in the text. **(d)** Cross section showing the main alteration minerals present and base-metal mineralization. Dashed lines reflect the interpreted geology illustrated in Figure 5c.

Figure 7. Representative photographs of the main lithologies observed and styles of hydrothermal alteration present at King. (a-b) Variably banded and sheared footwall garnet-amphibolite. (c) Intensely chloritized zone of footwall amphibolite containing disseminated magnetite. (d) Anthophyllite-bearing schist from the mixed footwall sequence. (e-f) Folded and banded schist from the mixed footwall sequence with individual layers composed almost entirely of quartz, muscovite and epidote. (g) Albite-rich schists from the mixed footwall sequence. (h) Intensely silicified footwall felsic rocks (quartz-muscovite schist). (i) Finely banded quartz-biotite/amphibole±garnet schists from the stratigraphic hanging-wall of the deposit. Note the variation in rock types and alteration. (j) Finely banded silicified hanging-wall schists. (k) Polymict volcanic breccia with clasts of surrounding lithologies. (l) Possible grading in drillhole EC056D (hanging-wall strata), with coarse bases and

schists fining downhole. (m) Early quartz-feldspar porphyry sill intruding the King deposit stratigraphy (sample GK024; **Fig. 6c** labelled 1). (n) Late unaltered quartz-feldspar porphyry sill intruding the King deposit stratigraphy (**Fig. 6c** labelled 2). (o) Basaltic dyke most likely from the Palaeoproterozoic Widgiemooltha Dyke Suite cutting the footwall garnet-amphibolite. Varioles are often present near upper and lower contacts.

Figure 8. Representative drillcore photographs of the main styles of sulfide mineralization observed at the King deposit. (a) Stringer sulfide mineralization in the chloritic zone of the footwall garnet-amphibolite, dominated by pyrrhotite with lesser chalcopyrite. (b) Blebby and stringer chalcopyrite-pyrite mineralization in footwall-garnet amphibolite. (c) Folded pyrite-sphalerite veins within the footwall quartz-muscovite schist. (d) Contact between the quartz-muscovite schist and stratigraphically overlying massive sulfides (dominated by pyrite with lesser replacive sphalerite). (e) Cap of massive Fe-sulfides (dominated by pyrite and pyrrhotite) containing milled fragments of footwall and hanging-wall strata. (f) Recrystallized pyritic stringers in banded hanging-wall schists. (g) Stringers of coarse euhedral pyrite in hanging-wall schists directly overlying massive sulfides. Tightly folded and sheared, pyrite-rich hanging-wall schists. (i) Fault gouge within the thin (<30cm) zone of massive sulfides in northernmost diamond drillhole EC063D.

Figure 9. Photomicrographs, SEM images and chemical maps for representative samples from the King stratigraphy. (a) Footwall garnet-amphibolite with disseminated sulfides. (b) Reflected light image of sulfide and oxide phases present within footwall garnet-amphibolites (c) Chemical map of the area in Figure 8b (denoted by a white box). (d) Intensely chloritized zone of garnet-amphibolites. (e) Quartz-hornblende schist from the mixed footwall sequence (f-h) Anthophyllite bearing quartz-biotite-chlorite-albite-epidote schist from the mixed footwall sequence. (i-j) Quartz-muscovite schist from the immediate footwall of the King deposit. (k) Coarse euhedral pyrite in quartz-muscovite schist, with interstitial sphalerite. (l) Massive sulfide with sphalerite replacing pyrite and large milled clasts of surrounding quartz-muscovite schist. (m-n) Massive sulfides containing garnet porphyroblasts retrograded to chlorite. (o-r) Petrographic and SEM images of hanging-wall mafic (o,r) and felsic (p-q) strata. Drillhole numbers and sample depths are indicated by the format 116/425m. *Plane polarised light* – **Fig. 9a,f**; *Cross polarized light* – **Fig. 9d,e,i,j,o,p,q**; *SEM images* – **Fig. 9g,k,m,r**. *SEM composite chemical maps* - **Fig. 9c,h,n**. Chemical mapping was completed using a Hitachi TM3030Plus Tabletop Scanning Electron Microscope at University College Dublin, Ireland. Maps were completed over 2-3 hours each using a pixel dwell time of 800µs, resolution of 1024 and process time of 4 seconds. Composite colour maps were produced by merging element concentration maps of interest using the Oxford Instruments Aztec One (v. 3.2) software.

Figure 10. Immobile element geochemistry for samples analysed from the King deposit. (a-c) Zr/TiO_2 vs Nb/Y discrimination diagrams for volcanic rocks (after Pearce, 1996). Probability ellipses for various rock types are shown after Pearce (1996). These represent 10% probability contours – that is 10% of samples from that group will plot outside the respective contour. (d) Th vs Co discrimination diagram of Hastie et al. (2007). (e-f) VHMS fertility diagrams of Lesher et al (1986; Fig. 9d) and Hart et al (2004; Fig. 9f). Felsic volcanic rocks from Teutonic Bore are of FIII affinity characterised by high concentrations of the HFSE and low Zr/Y and La/Yb ratios. Footwall quartz-muscovite schist from King is of FI to FII affinity and less prospective for VHMS mineralization. (g) Th/Yb vs Nb/Yb diagram of Pearce (2008, 2014). Arc related volcanic rocks will parallel the mantle array, whereas samples trending obliquely to it are associated with crustal contamination (Pearce, 2008). 1. Yilgarn Felsic Intrusion (Hayman et al. 2015b); 2. Felsic Archean Crust (Rudnick & Fountain, 1995); 3. Upper Continental Crust (Taylor & Mclennan, 1995).

Figure 11. Chondrite-normalized REE profiles (after McDonough & Sun, 1995) for samples analysed from the King deposit. Shaded fields for rocks from Nimbus and Teutonic Bore are from Hollis et al. (2017) and Hollis (unpublished) respectively.

Figure 12. Mobile element geochemistry of samples analysed from King. The Box Plot (bottom left) uses both the Alteration Index (A.I.) of Ishikawa et al. (1976) and the Carbonate-chlorite-pyrite Index of Large et al. (2001a) to show common trends associated with hydrothermal alteration. A.I.=100*(K_2O+MgO)/(K_2O+MgO+Na_2O+CaO);
CCPI=100*(MgO+FeO)/(MgO+FeO+Na_2O+K_2O).

Figure 13. Downhole geochemical profiles for drillholes EC116D, EC056D and EC031D using data obtained by both the pXRF and whole rock methods (see **Figure 6** for drillhole locations). Eu/Eu^* calculated after Boynton (1984).

Figure 14. Prospectivity of felsic rocks from (a) the Abitibi greenstone belt, Canada, and (b) Younami Terrane, and Eastern Goldfields, according to the Zr/Y vs Y felsic discrimination diagram of Lesher et al. (1986). All stacked plots are the same scale with Zr/Y ratios for each section of the stack indicated on y-axes. Adapted from Hollis et al. (2015), with additional data from Hollis et al. (2017a – Nimbus deposit) and Hassan (2017a – Wheatley deposit).

Figure 15. (a) Chemographic diagrams (A'CF, A'KF and AFM) used to portray common alteration trends and mineral nodes in metamorphosed terranes (diagrams modified after Bonnet & Corriveau, 2007; Corriveau & Spry, 2014). Samples are plotted using molecular proportions (i.e. the chemical analysis of the rock is recalculated by dividing the molecular weight of each oxide constituent by the molecular weight of that oxide). (a) King deposit, (b-c) Mafic and felsic volcanic rocks analysed from the Teutonic Bore and Wheatley VHMS deposits (data from Hollis, unpublished; Hassan, 2017a). The point density contours in 14b reflect the field of least/weakly-altered felsic and intermediate volcanic/volcaniclastic rocks from the Yilgarn Craton. This dataset, compiled by Hollis et al. (2015), was filtered to remove samples with anomalous Zn (>100 ppm) and high degrees of alteration (Silicification Index >80%). A'CF: A'=Al_2O_3+Fe_2O_3-(K_2O+Na_2O), C=CaO, F=FeO+MnO+MgO. A'KF: A=Al_2O_3+Fe_2O_3-(K_2O+Na_2O+CaO), K=K2O, F=FeO+MnO+MgO. AFM: A=Al_2O_3-K_2O; F=FeO, M=MgO. Abbreviations for mineral names (Whitney and Evans, 2010): Act - actinolite, Alm - almandine (garnet), An - anorthite, Ath - anthophyllite, Bt - biotite, Cal - calcite, Chl - chlorite, Crd - cordierite, Di - diopside, Ep - epidote, Grs - grossular (garnet), Grt - garnet, Hbl - hornblende, Hd - hedenbergite, Kfs - K-feldspar, Ky - kyanite, Ms - muscovite, Opx - orthopyroxene, Prp - pyrope (garnet), Sil - sillimanite, Tr – tremolite.

Figure 16. Geochemical and mineralogical vectors to mineralization at King, plotted as distance to massive sulfide mineralization (calculated perpendicular to ore in section 6538650mN; **Fig. 6c**). Normative CIPW quartz and cordierite abundances (volume %) were determined using the Norm 4 spreadsheet of Kurt Hollocher (Union College).

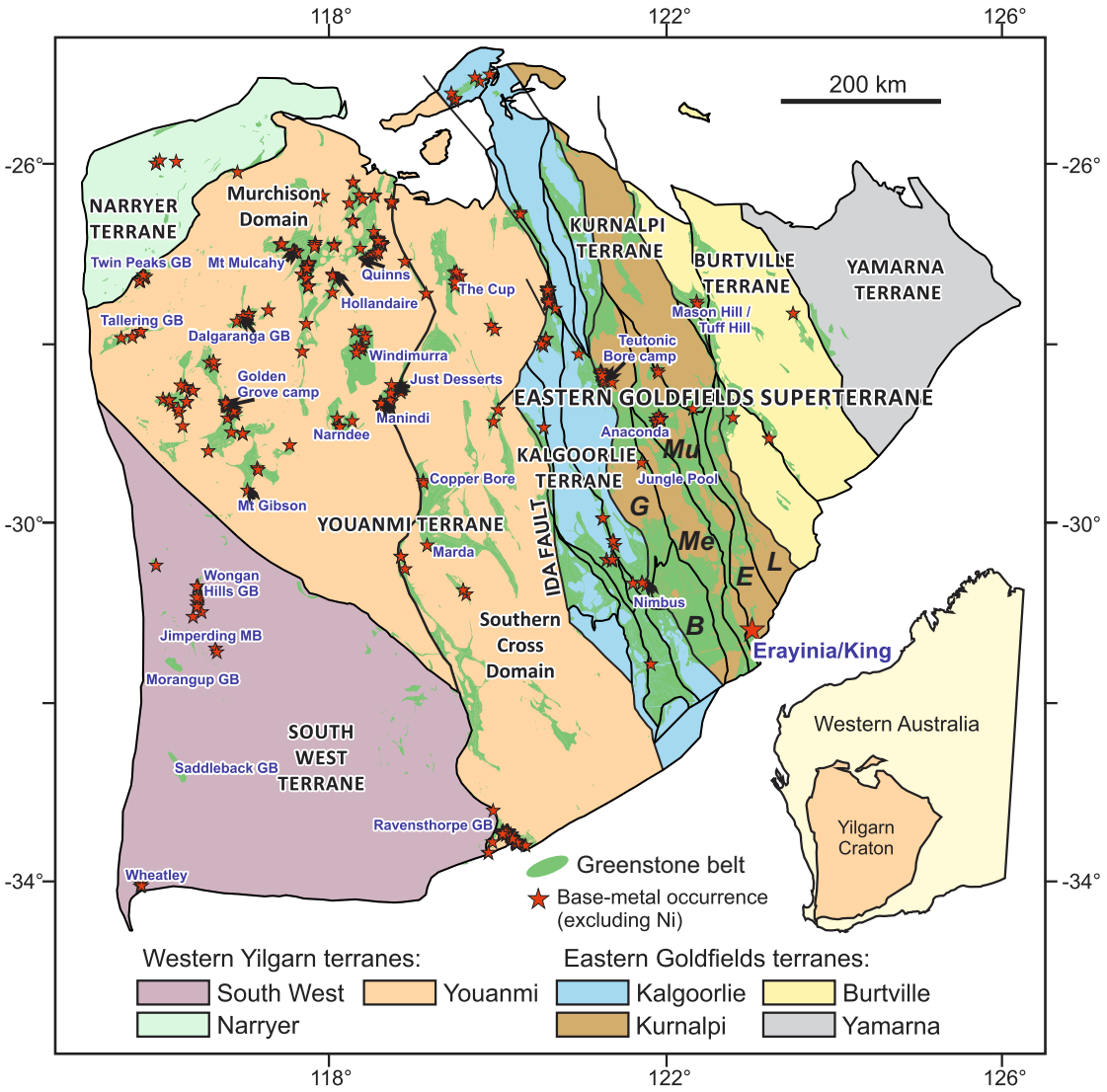
118°
122°
126°
-26°
-30°
-34°
200 km
NARRYER TERRANE
Murchison Domain
Twin Peaks GB
Mt Mulcahy
Quinns
The Cup
Hollandaire
Tallering GB
Dalgaranga GB
Windimurra
Golden Grove camp
Just Desserts
Manindi
Narndee
Mt Gibson
YOUANMI TERRANE
Marda
Copper Bore
KURNALPI TERRANE
BURTVILLE TERRANE
YAMARNA TERRANE
Mason Hill / Tuff Hill
Teutonic Bore camp
EASTERN GOLDFIELDS SUPERTERRANE
Anaconda
KALGOORLIE TERRANE
Jungle Pool
IDA FAULT
Nimbus
Erayinia/King
Wongan Hills GB
Jimperding MB
Morangup GB
Southern Cross Domain
SOUTH WEST TERRANE
Saddleback GB
Ravensthorpe GB
Wheatley
Western Australia
Yilgarn Craton
Greenstone belt
Base-metal occurrence (excluding Ni)
Western Yilgarn terranes:
South West
Youanmi
Narryer
Eastern Goldfields terranes:
Kalgoorlie
Kurnalpi
Burtville
Yamarna

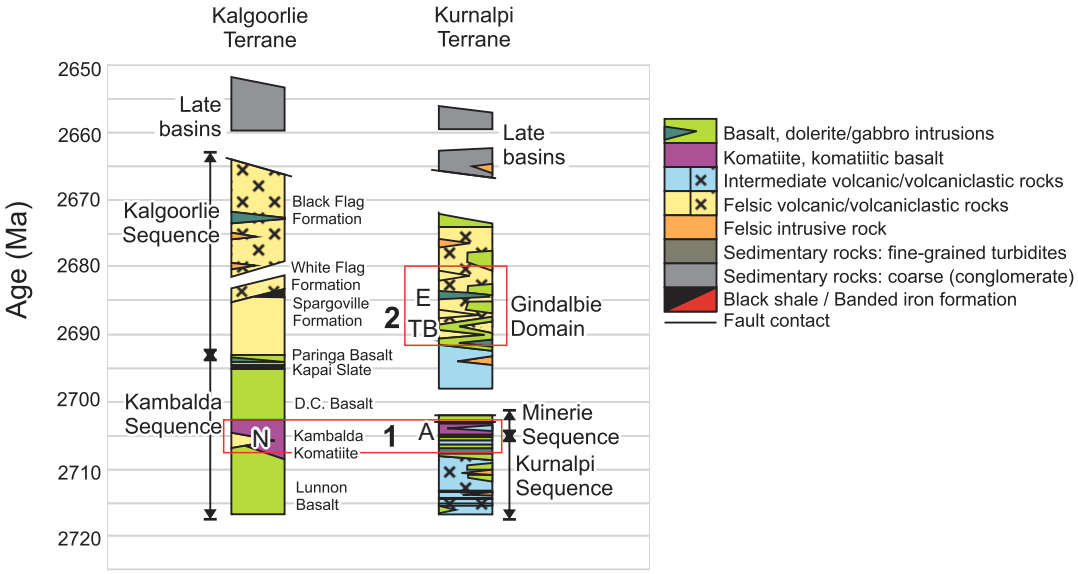
Kalgoorlie Terrane
Kurnalpi Terrane
Age (Ma)
2650
2660
2670
2680
2690
2700
2710
2720
Late basins
Kalgoorlie Sequence
Black Flag Formation
White Flag Formation
Spargoville Formation
Paringa Basalt
Kapai Slate
Kambalda Sequence
D.C. Basalt
N
Kambalda Komatiite
Lunnon Basalt
1
2
E
TB
A
Late basins
Gindalbie Domain
Minerie Sequence
Kurnalpi Sequence
Basalt, dolerite/gabbro intrusions
Komatiite, komatiitic basalt
Intermediate volcanic/volcaniclastic rocks
Felsic volcanic/volcaniclastic rocks
Felsic intrusive rock
Sedimentary rocks: fine-grained turbidites
Sedimentary rocks: coarse (conglomerate)
Black shale / Banded iron formation
Fault contact

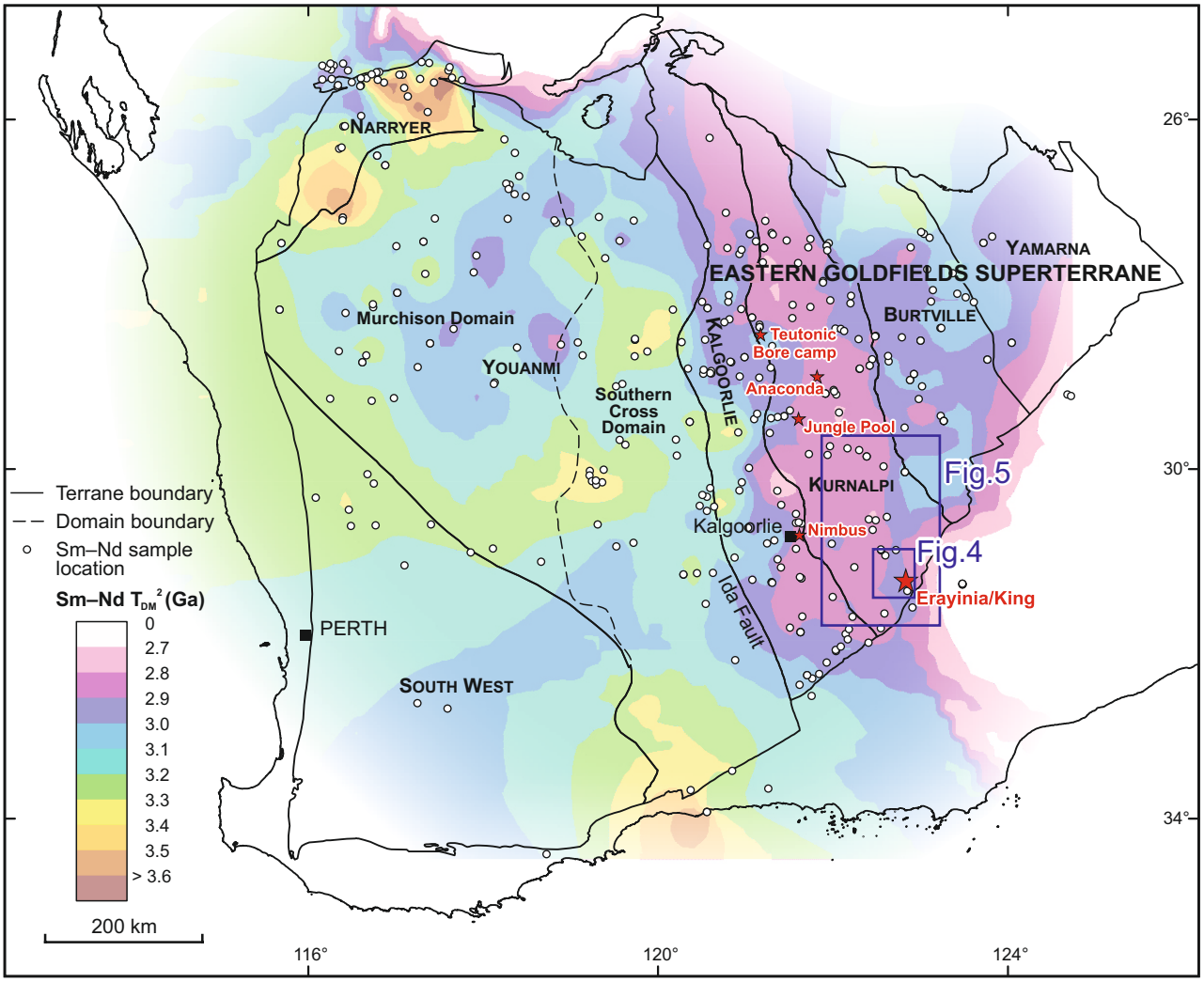
NARRYER
EASTERN GOLDFIELDS SUPERTERRANE
YAMARNA
BURTVILLE
Murchison Domain
YOUANMI
Southern Cross Domain
KALGOORLIE
Teutonic Bore camp
Anaconda
Jungle Pool
KURNALPI
Fig.5
Fig.4
Kalgoorlie
Nimbus
Erayinia/King
Ida Fault
PERTH
SOUTH WEST
Terrane boundary
Domain boundary
Sm–Nd sample location
Sm–Nd T$_{DM}^{2}$ (Ga)
0
2.7
2.8
2.9
3.0
3.1
3.2
3.3
3.4
3.5
> 3.6
200 km
26°
30°
34°
116°
120°
124°

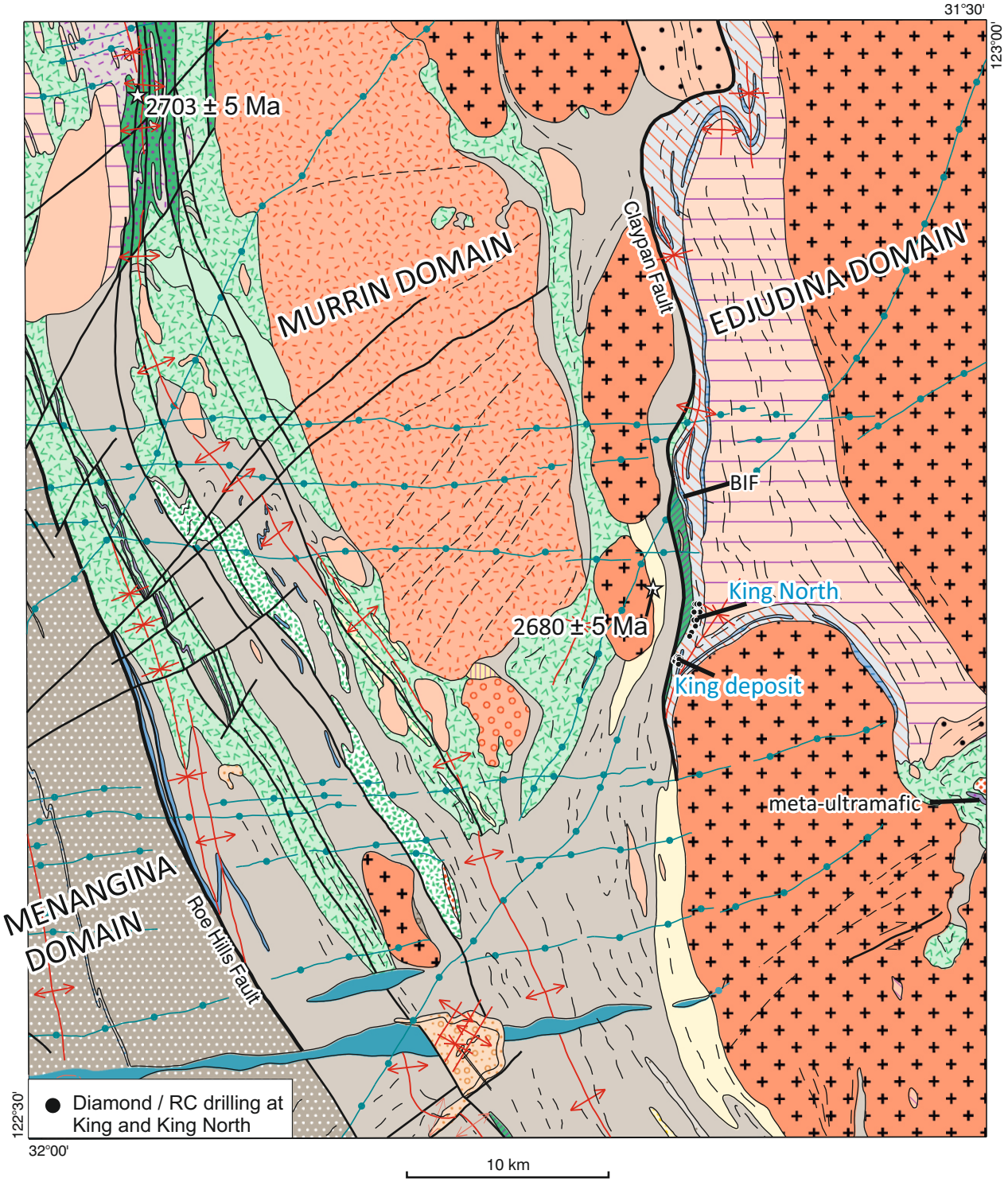

Trend of bedding or foliation
Anticline
Syncline
Fault, showing relative dextral horizontal displacement

Woodline Formation
Quartz sandstone; minor conglomerate

Dolerite dyke, sill, and plug

Widgiemooltha Dyke Suite
Binneringie Dyke

Erayinia Granitic Suite
Quartz monzonite; commonly porphyritic
Porphyritic quartz monzonite

Schist derived from granitic rock
Foliated granitic rock interleaved with subordinate foliated mafic rock

Granitic rock, undivided; includes deeply weathered rock
Quartz monzonite; commonly porphyritic
Fine-grained quartz monzonite
Quartz-rich monzogranite

Schist

Mount Belches Formation
Shale; metamorphosed
Chert; metamorphosed

Para-amphibolite

Sedimentary rock, undivided; includes sandstone, siltstone, shale and chert; metamorphosed
Conglomerate with subordinate sandstone; matrix or clast supported; metamorphosed
Sandstone derived from mafic rocks; metamorphosed

Chert and banded chert; locally includes silicified (black) shale, or slate; metamorphosed
Chert and banded chert; ferruginous; locally includes silicified (black) shale, slate, or exhalite; metamorphosed

Quartzofeldspathic micaceous schist derived from felsic volcanic or volcaniclastic protolith

Andesite, commonly with plagioclase and/or hornblende phenocrysts; metamorphosed
Quartz–feldspar porphyritic rock; weak to schistose foliation; metamorphosed
Rhyolitic volcaniclastic rock; metamorphosed

Amphibolite, fine to medium grained; commonly weakly foliated or massive
Foliated, fine-grained metamafic rock

Fine- to very fine-grained mafic rock; metamorphosed
Basalt; locally porphyritic; includes dolerite-textured zones; metamorphosed
Basalt with volcaniclastic textures; metamorphosed

Meta-ultramafic rock, undivided; includes talc–chlotite (–carbonate) and tremolite–chlorite schist

YILGARN CRATON

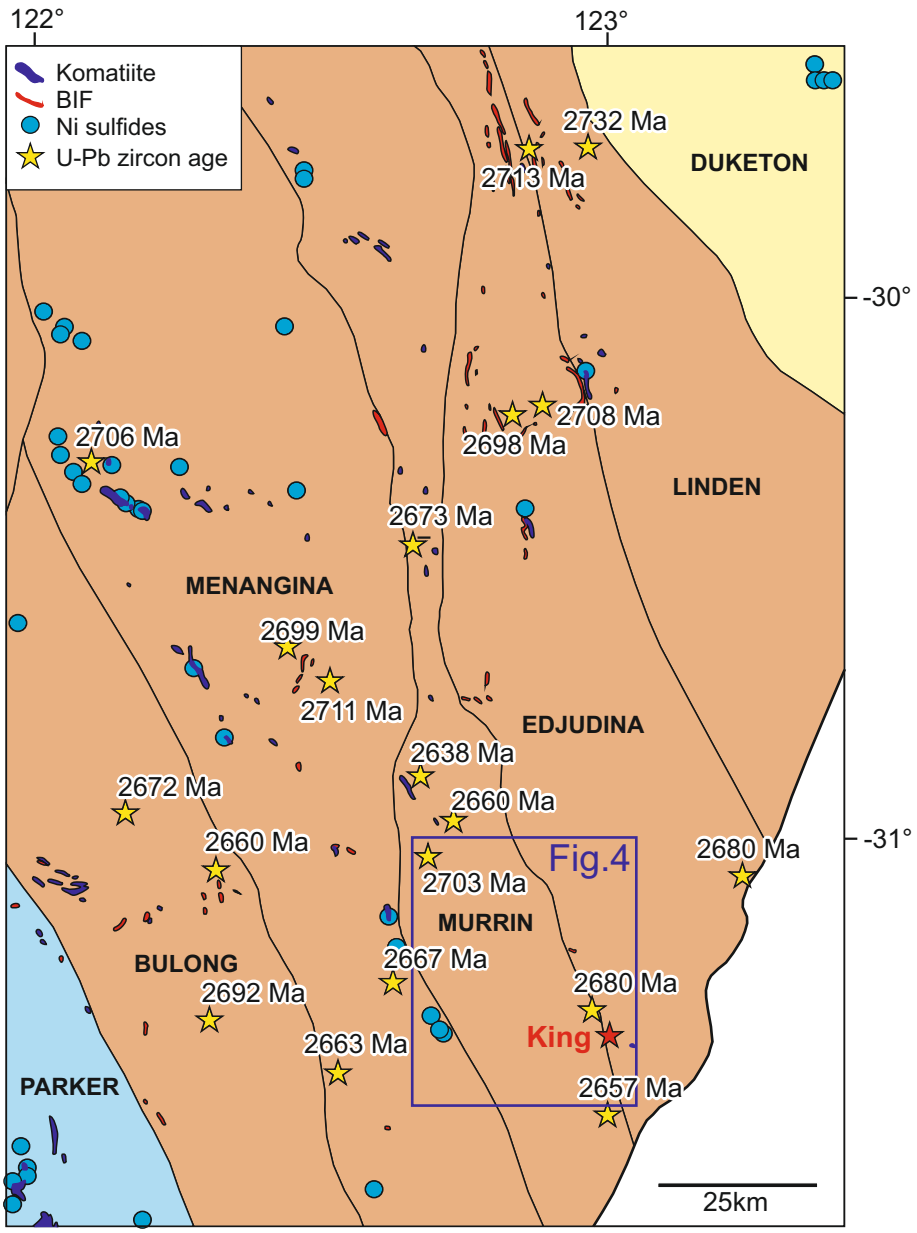
122°
123°
-30°
-31°
Komatiite
BIF
Ni sulfides
U-Pb zircon age
2732 Ma
2713 Ma
DUKETON
2708 Ma
2698 Ma
2706 Ma
LINDEN
2673 Ma
MENANGINA
2699 Ma
2711 Ma
EDJUDINA
2638 Ma
2672 Ma
2660 Ma
2660 Ma
2680 Ma
Fig.4
2703 Ma
MURRIN
2667 Ma
BULONG
2692 Ma
2680 Ma
King
2663 Ma
PARKER
2657 Ma
25km

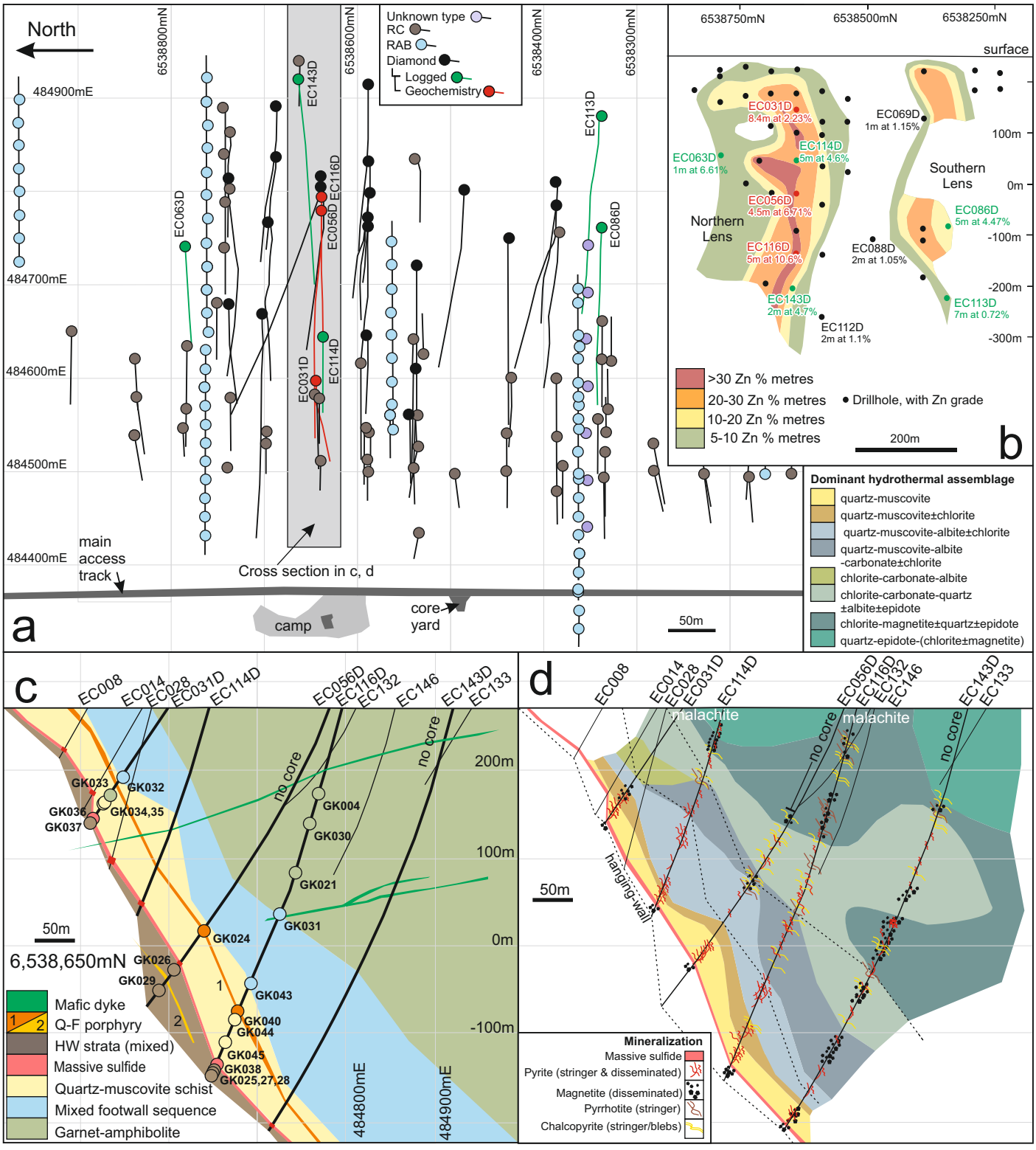
North
6538800mN
6538600mN
6538400mN
6538300mN
484900mE
484700mE
484600mE
484500mE
484400mE
Unknown type
RC
RAB
Diamond
Logged
Geochemistry
EC143D
EC116D
EC063D
EC056D
EC114D
EC031D
EC113D
EC086D
main access track
Cross section in c, d
camp
core yard
50m
a
6538750mN
6538500mN
6538250mN
surface
EC031D
8.4m at 2.23%
EC114D
5m at 4.6%
EC063D
1m at 6.61%
EC069D
1m at 1.15%
Southern Lens
Northern Lens
EC056D
4.5m at 6.71%
EC086D
5m at 4.47%
EC116D
5m at 10.6%
EC088D
2m at 1.05%
EC143D
2m at 4.7%
EC113D
7m at 0.72%
EC112D
2m at 1.1%
100m
0m
-100m
-200m
-300m
>30 Zn % metres
20-30 Zn % metres
10-20 Zn % metres
5-10 Zn % metres
Drillhole, with Zn grade
200m
b
Dominant hydrothermal assemblage
quartz-muscovite
quartz-muscovite±chlorite
quartz-muscovite-albite±chlorite
quartz-muscovite-albite -carbonate±chlorite
chlorite-carbonate-albite
chlorite-carbonate-quartz ±albite±epidote
chlorite-magnetite±quartz±epidote
quartz-epidote-(chlorite±magnetite)
c
EC008
EC014
EC028
EC031D
EC114D
EC056D
EC116D
EC132
EC146
EC143D
EC133
no core
200m
100m
0m
-100m
GK033
GK032
GK036
GK034,35
GK037
GK004
GK030
GK021
GK031
GK024
GK026
GK029
GK043
GK040
GK044
GK045
GK038
GK025,27,28
50m
6,538,650mN
484800mE
484900mE
Mafic dyke
Q-F porphyry
HW strata (mixed)
Massive sulfide
Quartz-muscovite schist
Mixed footwall sequence
Garnet-amphibolite
d
malachite
hanging-wall
50m
Mineralization
Massive sulfide
Pyrite (stringer & disseminated)
Magnetite (disseminated)
Pyrrhotite (stringer)
Chalcopyrite (stringer/blebs)

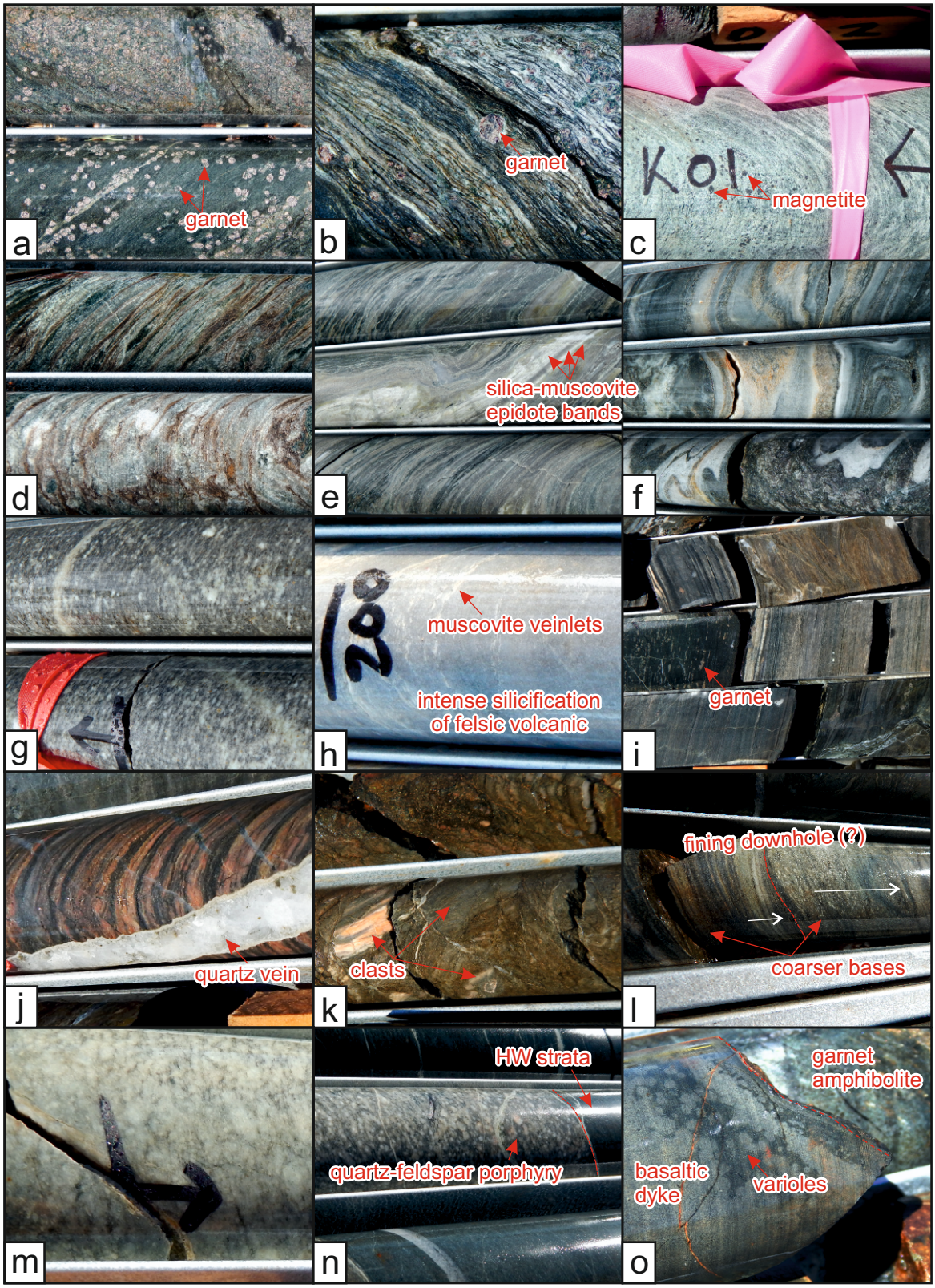
a
garnet
b
garnet
c
magnetite
d
e
silica-muscovite
epidote bands
f
g
h
muscovite veinlets
intense silicification
of felsic volcanic
i
garnet
j
quartz vein
k
clasts
l
fining downhole (?)
coarser bases
m
n
HW strata
quartz-feldspar porphyry
o
garnet
amphibolite
basaltic
dyke
varioles

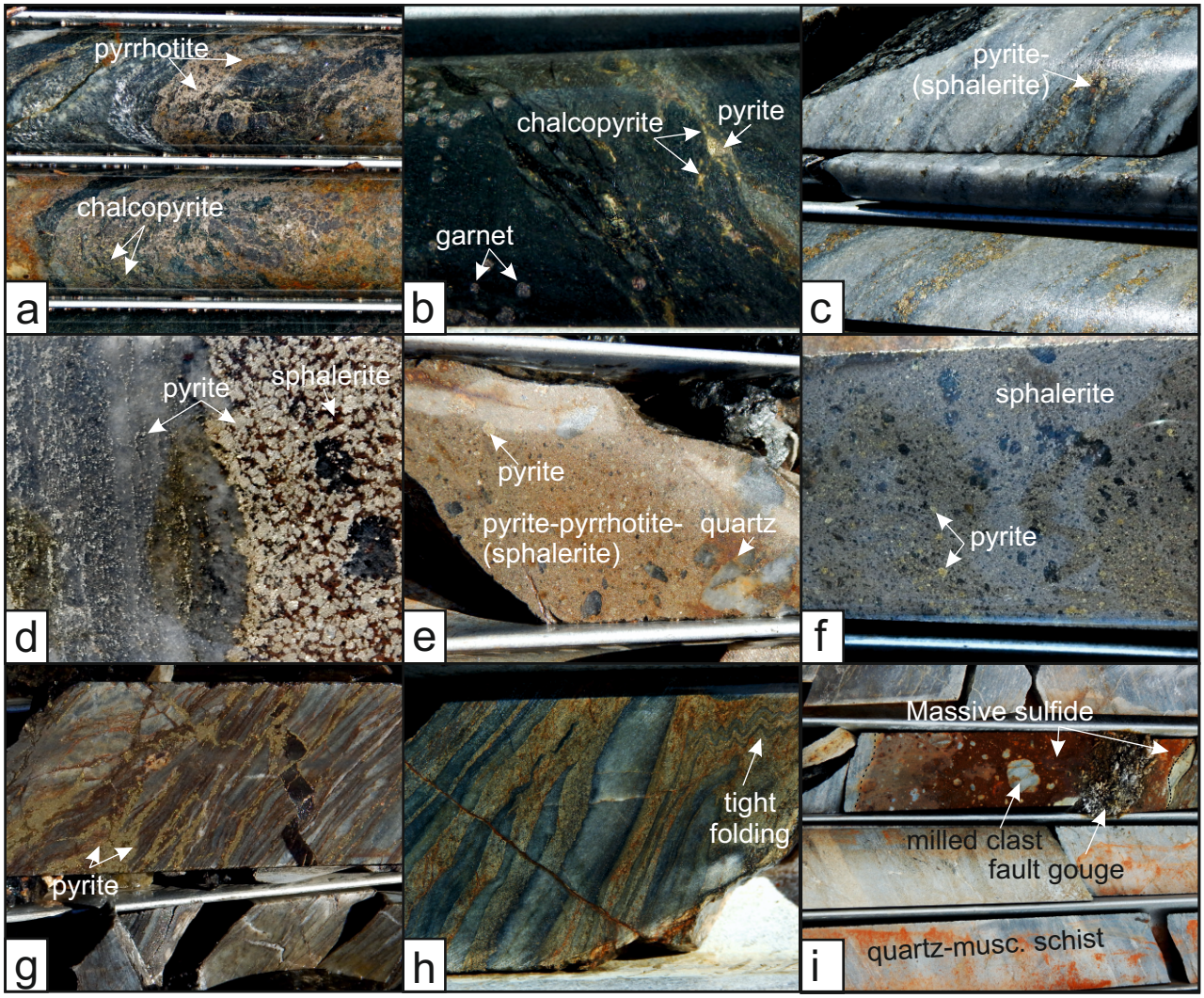
pyrrhotite
chalcopyrite
a
chalcopyrite
pyrite
garnet
b
pyrite-
(sphalerite)
c
pyrite
sphalerite
d
pyrite
pyrite-pyrrhotite-
(sphalerite)
quartz
e
sphalerite
pyrite
f
pyrite
g
tight
folding
h
Massive sulfide
milled clast
fault gouge
quartz-musc. schist
i

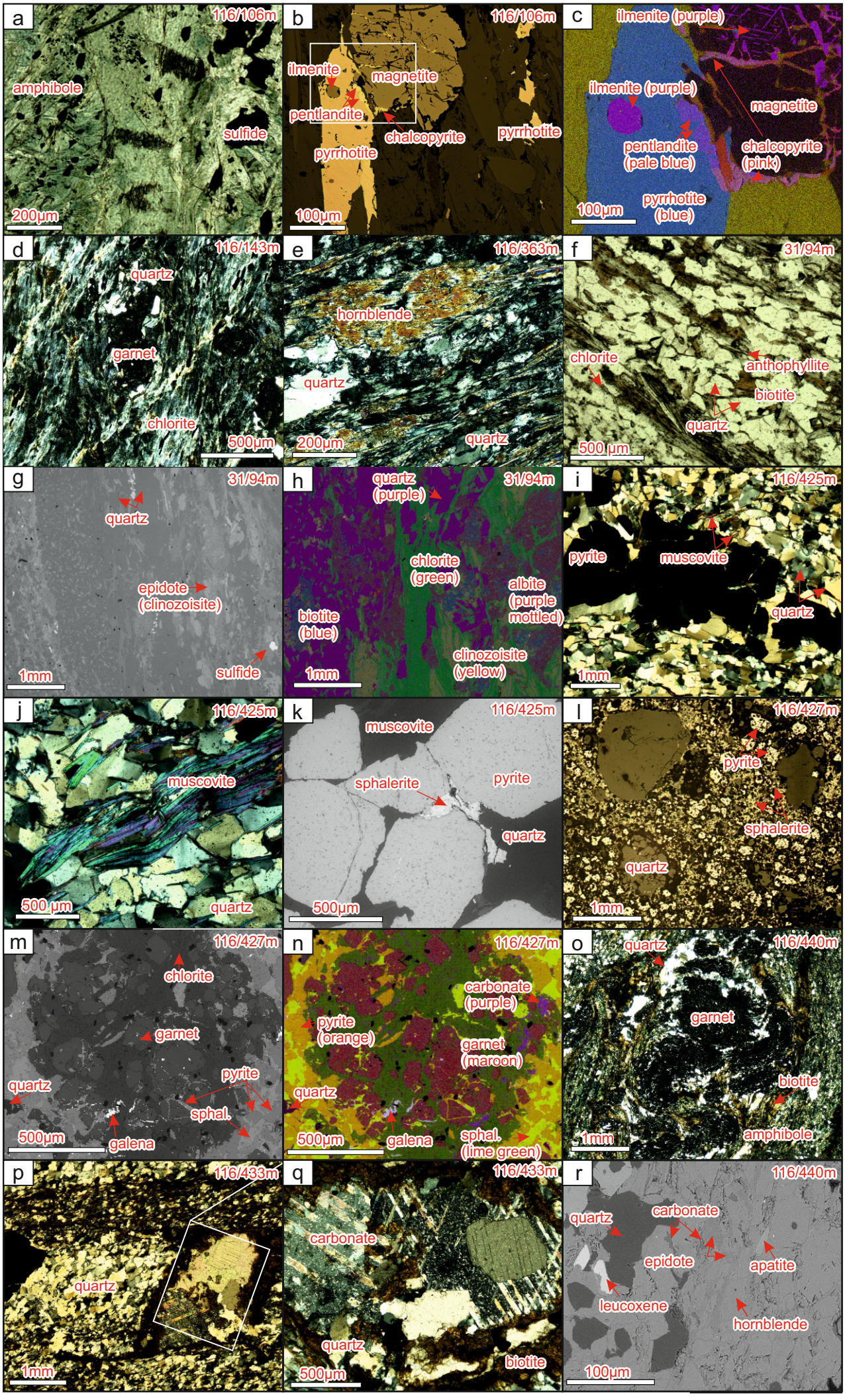
a
116/106m
amphibole
sulfide
200µm
b
116/106m
ilmenite
magnetite
pentlandite
chalcopyrite
pyrrhotite
pyrrhotite
100µm
c
ilmenite (purple)
ilmenite (purple)
magnetite
pentlandite
(pale blue)
chalcopyrite
(pink)
pyrrhotite
(blue)
100µm
d
116/143m
quartz
garnet
chlorite
500µm
e
116/363m
hornblende
quartz
200µm
quartz
f
31/94m
chlorite
anthophyllite
biotite
quartz
500 µm
g
31/94m
quartz
epidote
(clinozoisite)
1mm
sulfide
h
quartz
(purple)
31/94m
chlorite
(green)
albite
(purple
mottled)
biotite
(blue)
clinozoisite
(yellow)
1mm
i
116/425m
pyrite
muscovite
quartz
1mm
j
116/425m
muscovite
500 µm
quartz
k
116/425m
muscovite
sphalerite
pyrite
quartz
500µm
l
116/427m
pyrite
sphalerite
quartz
1mm
m
116/427m
chlorite
garnet
quartz
pyrite
sphal.
500µm
galena
n
116/427m
carbonate
(purple)
pyrite
(orange)
garnet
(maroon)
quartz
500µm
galena
sphal.
(lime green)
o
quartz
116/440m
garnet
biotite
1mm
amphibole
p
116/433m
quartz
1mm
q
116/433m
carbonate
quartz
500µm
biotite
r
116/440m
quartz
carbonate
epidote
apatite
leucoxene
hornblende
100µm

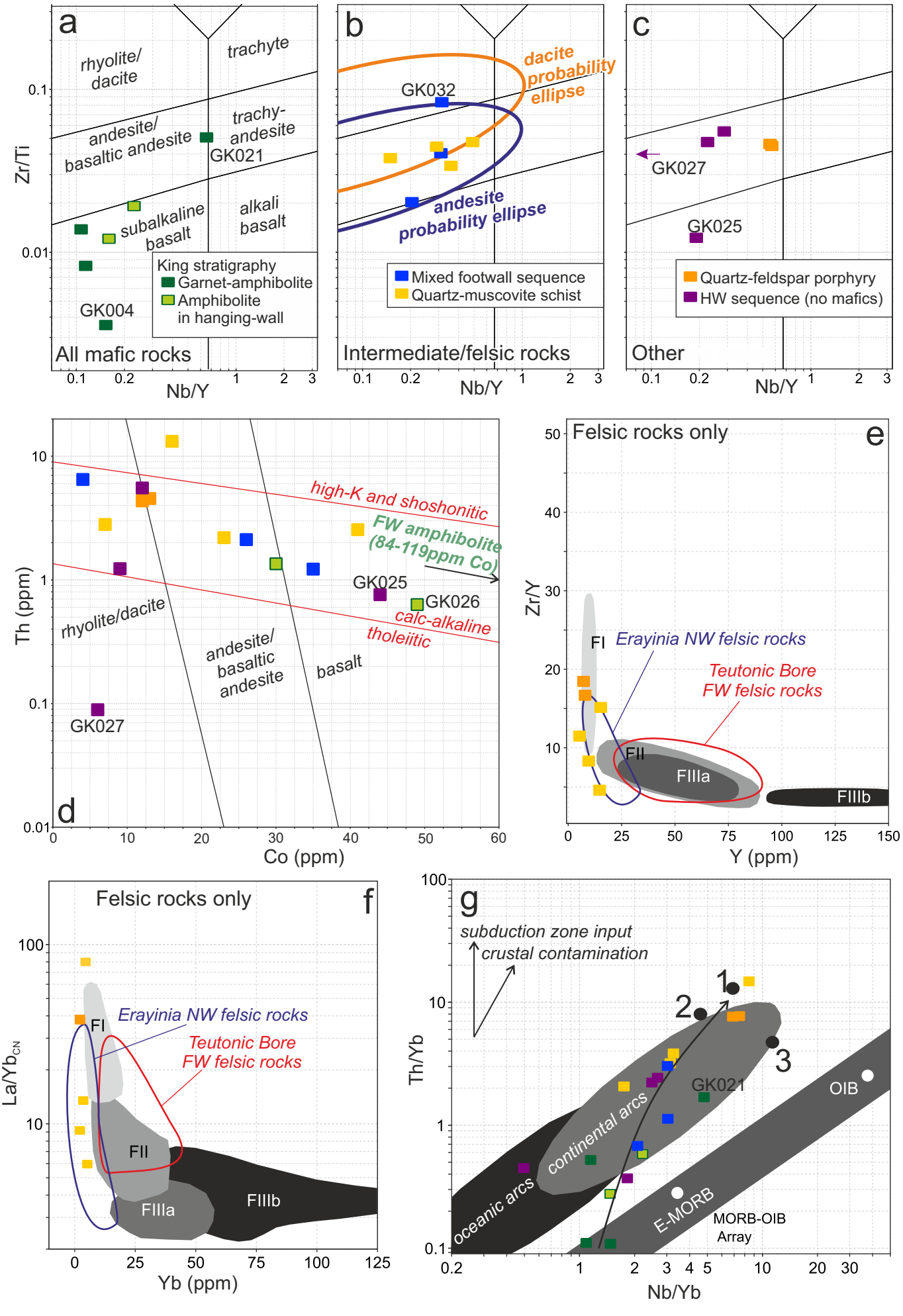
a
rhyolite/
dacite
trachyte
andesite/
basaltic andesite
trachy-
andesite
GK021
subalkaline
basalt
alkali
basalt
GK004
King stratigraphy
Garnet-amphibolite
Amphibolite
in hanging-wall
All mafic rocks
Zr/Ti
Nb/Y
b
GK032
dacite
probability
ellipse
andesite
probability ellipse
Mixed footwall sequence
Quartz-muscovite schist
Intermediate/felsic rocks
Nb/Y
c
GK027
GK025
Quartz-feldspar porphyry
HW sequence (no mafics)
Other
Nb/Y
d
high-K and shoshonitic
FW amphibolite
(84-119ppm Co)
GK025
GK026
calc-alkaline
tholeiitic
rhyolite/dacite
andesite/
basaltic
andesite
basalt
GK027
Th (ppm)
Co (ppm)
e
Felsic rocks only
Zr/Y
FI
Erayinia NW felsic rocks
Teutonic Bore
FW felsic rocks
FII
FIIIa
FIIIb
Y (ppm)
f
Felsic rocks only
La/Yb$_{CN}$
FI
Erayinia NW felsic rocks
Teutonic Bore
FW felsic rocks
FII
FIIIa
FIIIb
Yb (ppm)
g
subduction zone input
crustal contamination
1
2
3
GK021
continental arcs
oceanic arcs
OIB
E-MORB
MORB-OIB
Array
Th/Yb
Nb/Yb

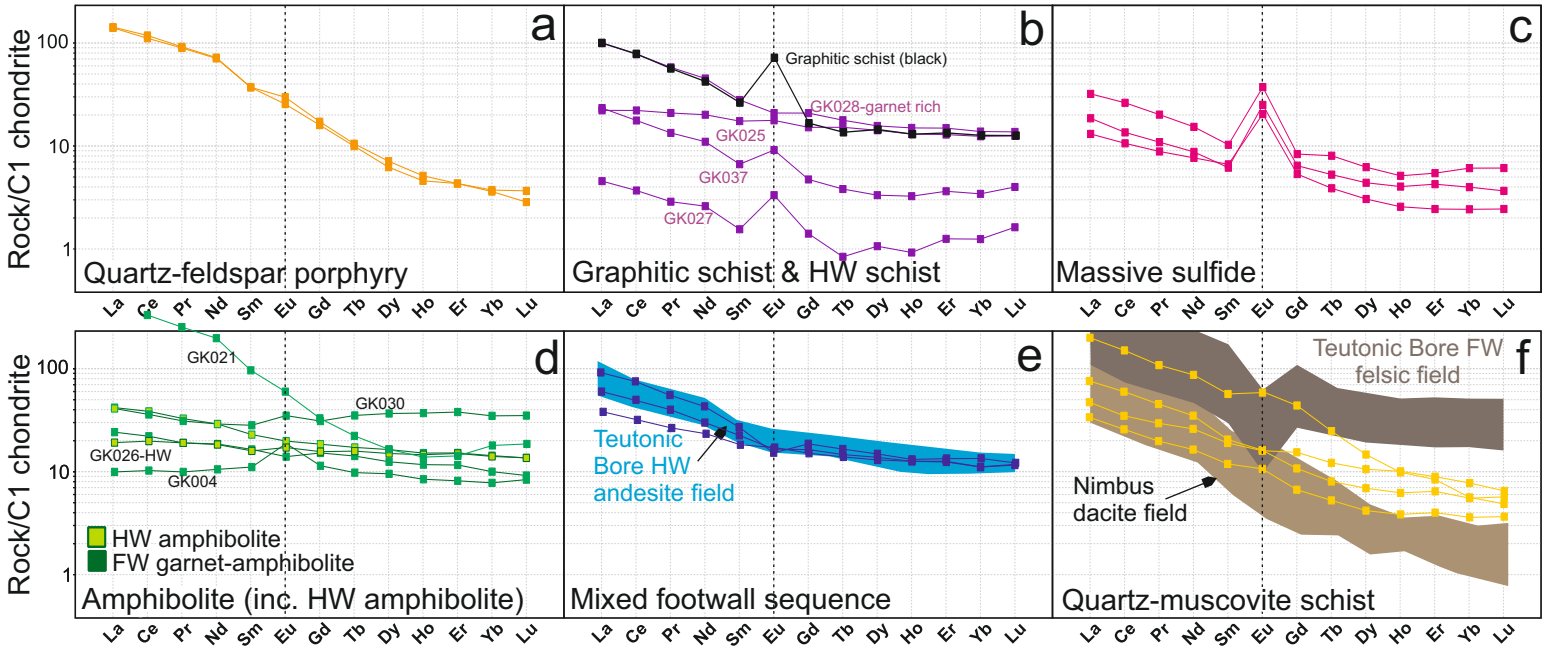
a
Quartz-feldspar porphyry
b
Graphitic schist & HW schist
Graphitic schist (black)
GK028-garnet rich
GK025
GK037
GK027
c
Massive sulfide
Rock/C1 chondrite
100
10
1
La Ce Pr Nd Sm Eu Gd Tb Dy Ho Er Yb Lu
d
Amphibolite (inc. HW amphibolite)
GK021
GK030
GK026-HW
GK004
HW amphibolite
FW garnet-amphibolite
e
Mixed footwall sequence
Teutonic
Bore HW
andesite field
f
Quartz-muscovite schist
Teutonic Bore FW
felsic field
Nimbus
dacite field

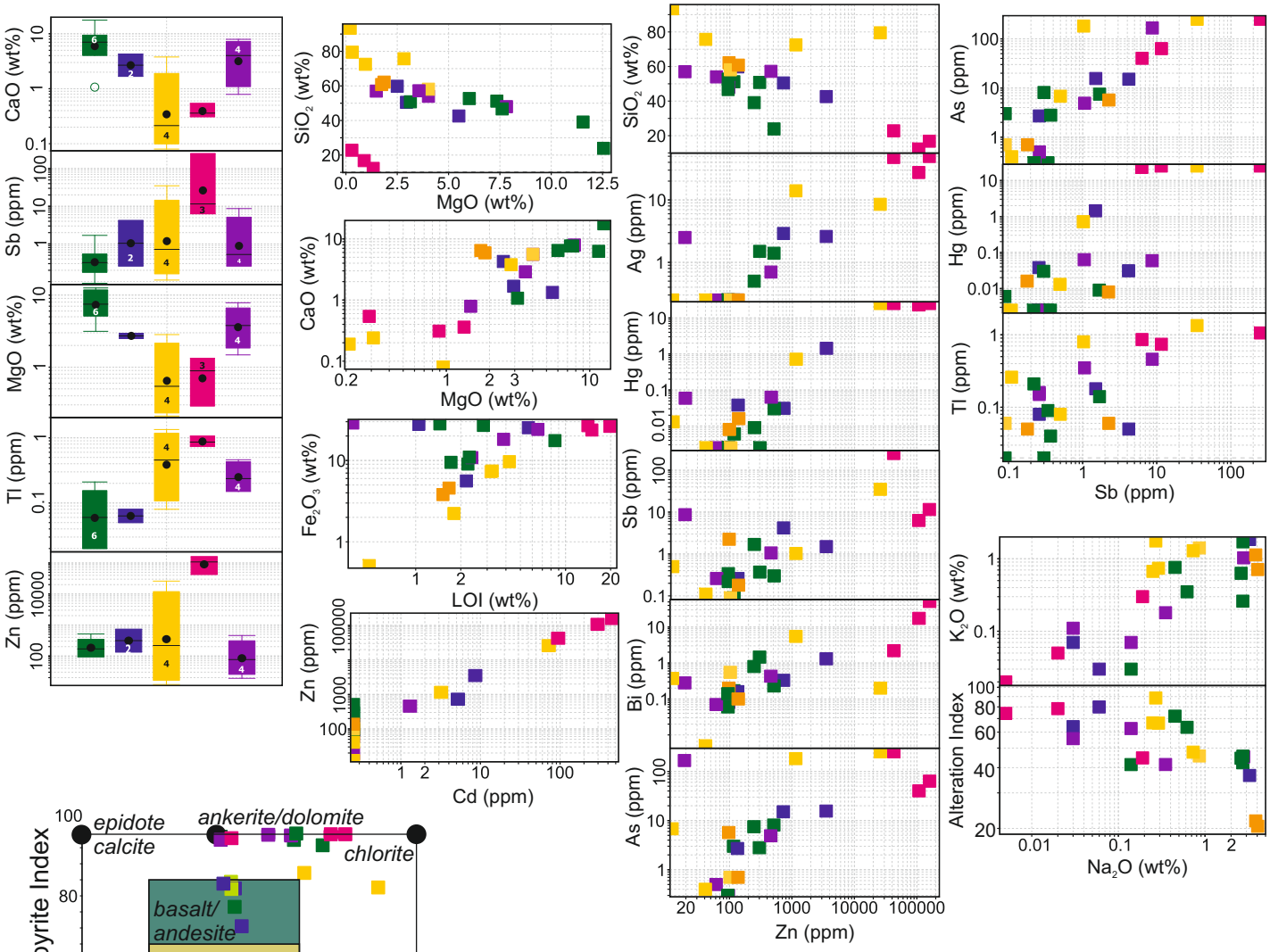
CaO (wt%)
Sb (ppm)
MgO (wt%)
Tl (ppm)
Zn (ppm)
SiO2 (wt%)
MgO (wt%)
CaO (wt%)
MgO (wt%)
Fe2O3 (wt%)
LOI (wt%)
Zn (ppm)
Cd (ppm)
SiO2 (wt%)
Ag (ppm)
Hg (ppm)
Sb (ppm)
Bi (ppm)
As (ppm)
Zn (ppm)
As (ppm)
Hg (ppm)
Tl (ppm)
Sb (ppm)
K2O (wt%)
Alteration Index
Na2O (wt%)

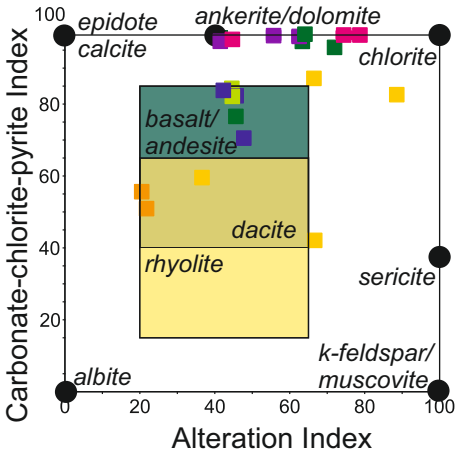
epidote
calcite
ankerite/dolomite
chlorite
basalt/
andesite
dacite
rhyolite
sericite
albite
k-feldspar/
muscovite
Carbonate-chlorite-pyrite Index
Alteration Index

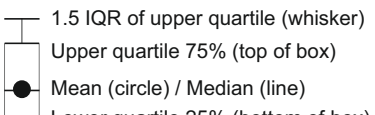
1.5 IQR of upper quartile (whisker)
Upper quartile 75% (top of box)
Mean (circle) / Median (line)
Lower quartile 25% (bottom of box)
1.5 IQR of lower quartile (whisker)

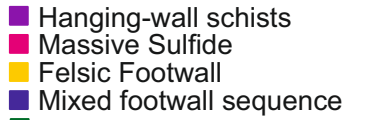
Hanging-wall schists
Massive Sulfide
Felsic Footwall
Mixed footwall sequence
Amphibolite
Quartz-feldspar porphyry sill

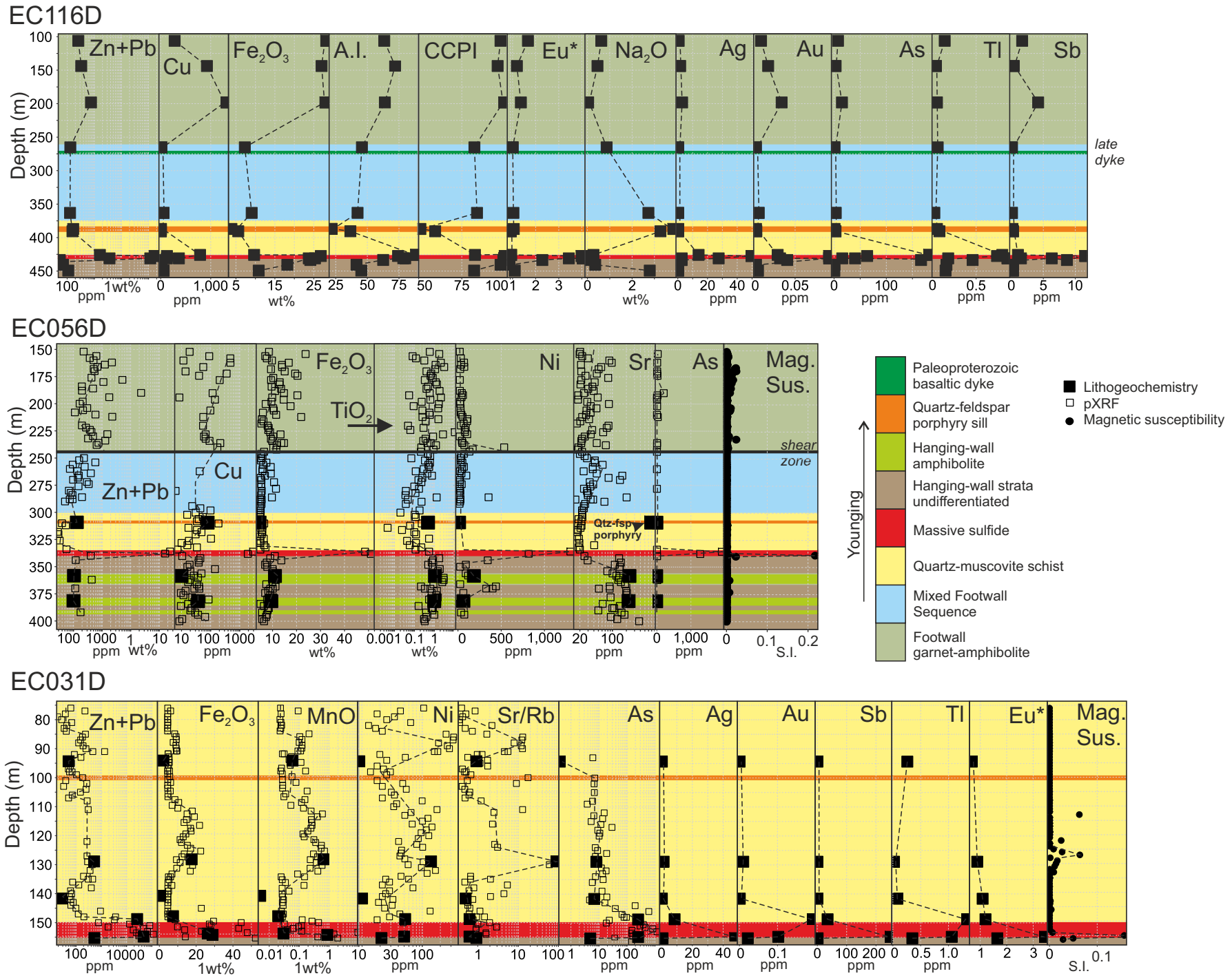
EC116D
Depth (m)
Zn+Pb
Cu
Fe2O3
A.I.
CCPI
Eu*
Na2O
Ag
Au
As
Tl
Sb
late dyke
EC056D
Fe2O3
TiO2
Ni
Sr
As
Mag. Sus.
shear zone
Zn+Pb
Cu
Qtz-fsp porphyry
Younging
Paleoproterozoic basaltic dyke
Quartz-feldspar porphyry sill
Hanging-wall amphibolite
Hanging-wall strata undifferentiated
Massive sulfide
Quartz-muscovite schist
Mixed Footwall Sequence
Footwall garnet-amphibolite
Lithogeochemistry
pXRF
Magnetic susceptibility
EC031D
Zn+Pb
Fe2O3
MnO
Ni
Sr/Rb
As
Ag
Au
Sb
Tl
Eu*
Mag. Sus.

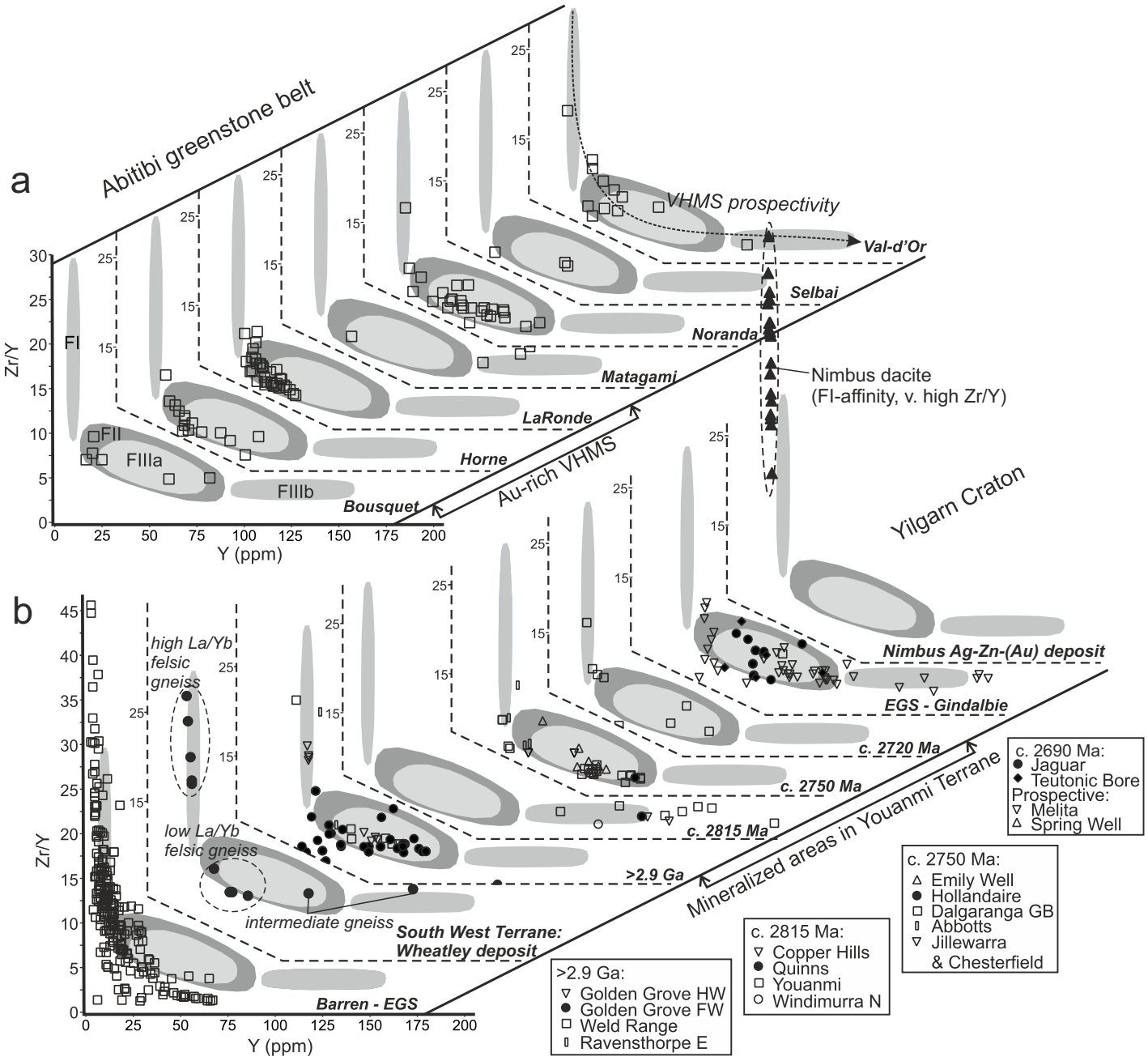
a
Abitibi greenstone belt
VHMS prospectivity
Val-d'Or
Selbai
Noranda
Matagami
LaRonde
Horne
Bousquet
Au-rich VHMS
Nimbus dacite
(FI-affinity, v. high Zr/Y)
FI
FII
FIIIa
FIIIb
Zr/Y
Y (ppm)
Yilgarn Craton
b
high La/Yb
felsic
gneiss
low La/Yb
felsic gneiss
intermediate gneiss
South West Terrane:
Wheatley deposit
Barren - EGS
Nimbus Ag-Zn-(Au) deposit
EGS - Gindalbie
c. 2720 Ma
c. 2750 Ma
c. 2815 Ma
>2.9 Ga
Mineralized areas in Youanmi Terrane
c. 2690 Ma:
Jaguar
Teutonic Bore
Prospective:
Melita
Spring Well
c. 2750 Ma:
Emily Well
Hollandaire
Dalgaranga GB
Abbotts
Jillewarra
& Chesterfield
c. 2815 Ma:
Copper Hills
Quinns
Youanmi
Windimurra N
>2.9 Ga:
Golden Grove HW
Golden Grove FW
Weld Range
Ravensthorpe E

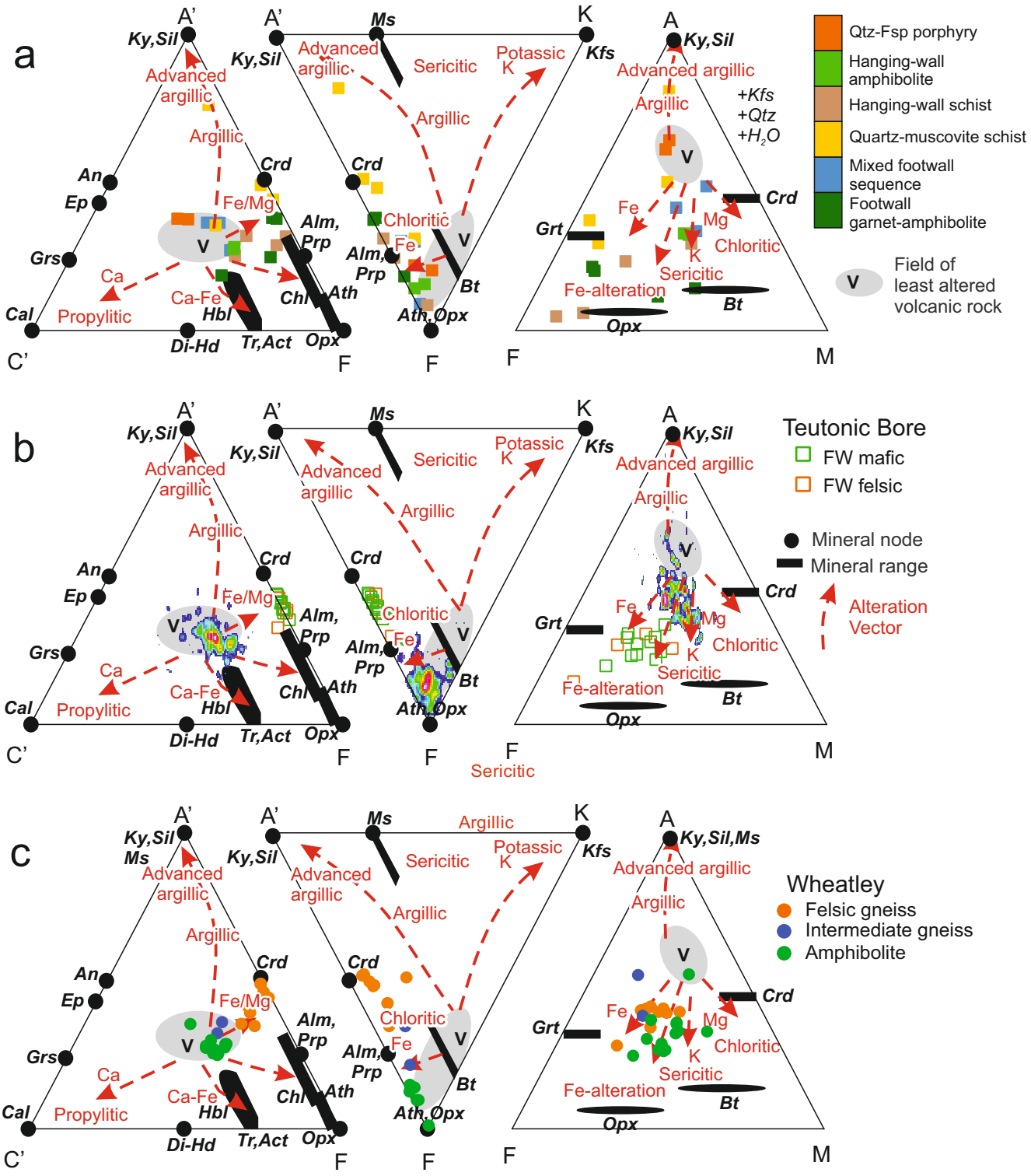
a
A'
Ky,Sil
Advanced argillic
Argillic
An
Ep
Grs
Cal
C'
Propylitic
Ca
Fe/Mg
Ca-Fe
Crd
Alm, Prp
Chl
Ath
Hbl
Tr,Act
Di-Hd
Opx
V
Ms
Sericitic
Potassic K
Kfs
Chloritic
Fe
Bt
Ath,Opx
F
K
A
+Kfs
+Qtz
+H2O
Grt
Mg
Fe-alteration
M
Qtz-Fsp porphyry
Hanging-wall amphibolite
Hanging-wall schist
Quartz-muscovite schist
Mixed footwall sequence
Footwall garnet-amphibolite
Field of least altered volcanic rock
b
Teutonic Bore
FW mafic
FW felsic
Mineral node
Mineral range
Alteration Vector
c
Wheatley
Felsic gneiss
Intermediate gneiss
Amphibolite
Ky,Sil,Ms

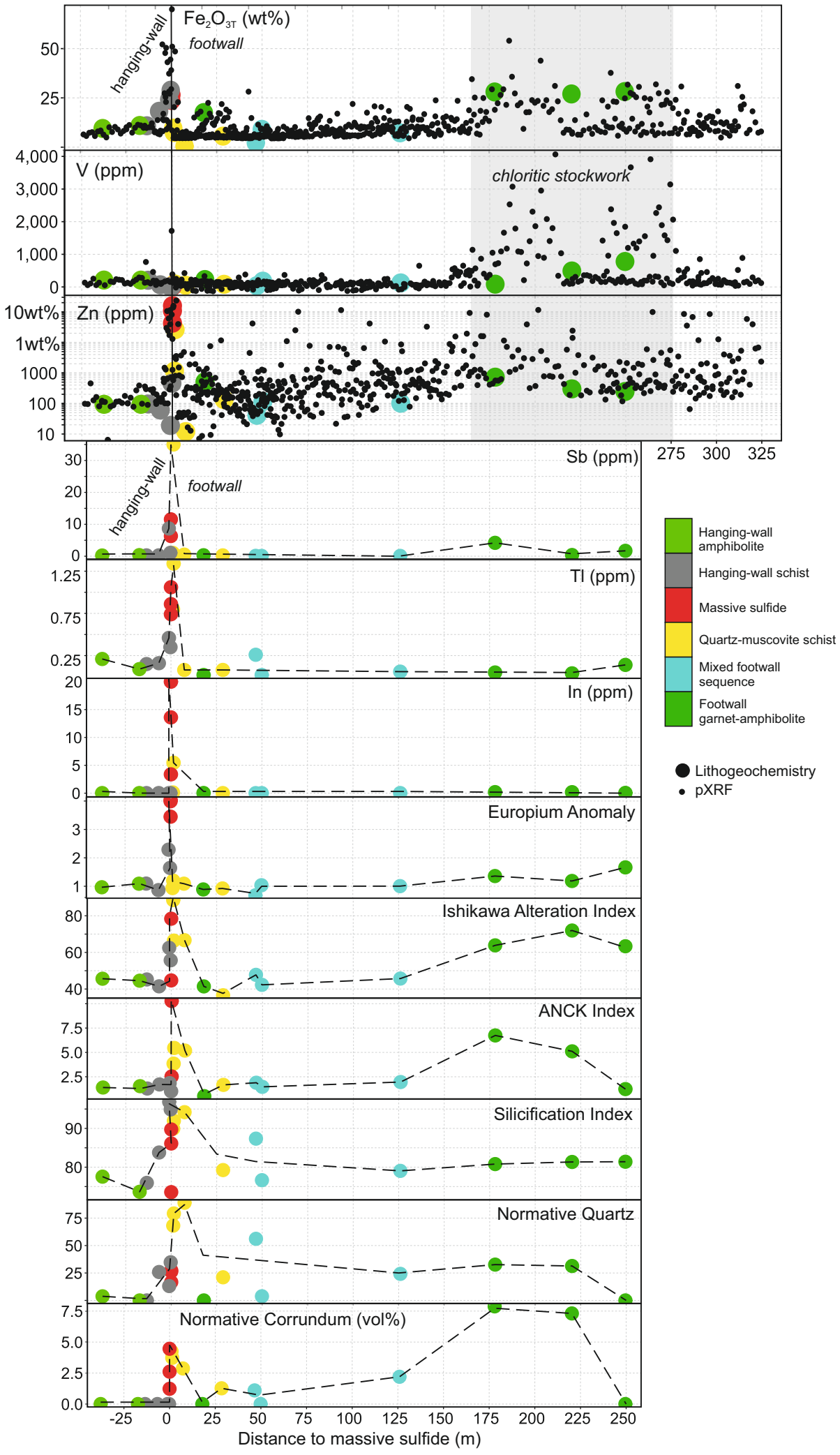
Fe_2O_{3T} (wt%)
hanging-wall
footwall
chloritic stockwork
V (ppm)
Zn (ppm)
10wt%
1wt%
Sb (ppm)
Tl (ppm)
In (ppm)
Europium Anomaly
Ishikawa Alteration Index
ANCK Index
Silicification Index
Normative Quartz
Normative Corrundum (vol%)
Distance to massive sulfide (m)
Hanging-wall amphibolite
Hanging-wall schist
Massive sulfide
Quartz-muscovite schist
Mixed footwall sequence
Footwall garnet-amphibolite
Lithogeochemistry
pXRF